

Optimization of BiVO₄ photoelectrodes made by electrodeposition for sun-driven water oxidation

Original

Optimization of BiVO₄ photoelectrodes made by electrodeposition for sun-driven water oxidation / Tolod, Kristine; Hernandez, Simelys; Castellino, Micaela; Deorsola, FABIO ALESSANDRO; Davarpanah, Elahe; Russo, Nunzio; Elahe, Davarpanah. - In: INTERNATIONAL JOURNAL OF HYDROGEN ENERGY. - ISSN 0360-3199. - 45:1(2020), pp. 605-618. [10.1016/j.ijhydene.2019.10.236]

Availability:

This version is available at: 11583/2770753 since: 2020-01-08T14:41:29Z

Publisher:

Elsevier

Published

DOI:10.1016/j.ijhydene.2019.10.236

Terms of use:

This article is made available under terms and conditions as specified in the corresponding bibliographic description in the repository

Publisher copyright

Elsevier postprint/Author's Accepted Manuscript

© 2020. This manuscript version is made available under the CC-BY-NC-ND 4.0 license
<http://creativecommons.org/licenses/by-nc-nd/4.0/>. The final authenticated version is available online at:
<http://dx.doi.org/10.1016/j.ijhydene.2019.10.236>

(Article begins on next page)

Original Article Published with Copyright (2019) by ELSEVIER

Citation Information:

Kristine Rodulfo Tolod, Simelys Hernández, Micaela Castellino, Fabio Alessandro Deorsola, Elahe Davarpanah, Nunzio Russo

Optimization of BiVO₄ photoelectrodes made by electrodeposition for sun-driven water oxidation

International Journal of Hydrogen Energy, 44 (2019), DOI:

<https://doi.org/10.1016/j.ijhydene.2019.10.236>.



Available online at www.sciencedirect.com

ScienceDirect

journal homepage: www.elsevier.com/locate/he



Optimization of BiVO₄ photoelectrodes made by electrodeposition for sun-driven water oxidation

Kristine Rodulfo Tolod ^{a,b}, Simelys Hernández ^{a,*}, Micaela Castellino ^a,
Fabio Alessandro Deorsola ^a, Elahe Davarpanah ^a, Nunzio Russo ^a

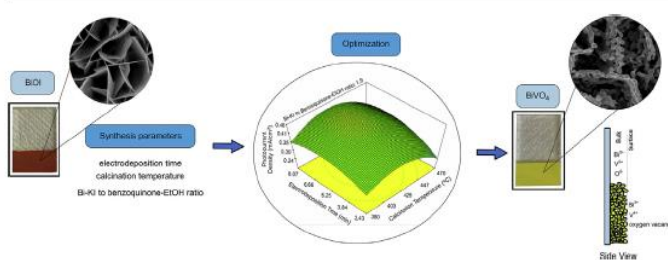
^a Department of Applied Science and Technology (DISAT), Politecnico di Torino, Corso Duca Degli Abruzzi, 10129, Turin, Italy

^b Université de Lyon, Institut de Chimie de Lyon, Laboratory of Chemistry, Catalysis, Polymers and Processes (C2P2, UMR 5265 - CNRS - University Claude Bernard Lyon 1 – Ecole Supérieure de Chimie Physique et Procédé CPE Lyon), Villeurbanne, France

HIGHLIGHTS

- Electrodeposition method of BiVO₄ was optimized by using Design of Experiments.
- The main physico-chemical properties influencing BiVO₄ photoactivity were identified.
- Depth profile XPS showed that the BiVO₄ surface is rich of V⁴⁺ while the bulk contains V⁵⁺.
- A higher amount of surface O vacancies is beneficial for the BiVO₄ photoactivity.

GRAPHICAL ABSTRACT



Optimization of BiVO₄ photoelectrodes made by electrodeposition for sun-driven water oxidation

Kristine Rodulfo Tolod^{a,b}, Simelys Hernández^{a,*}, Micaela Castellino^a, Fabio Alessandro Deorsola^a, Elahe Davarpanah^a and Nunzio Russo^a

^aDepartment of Applied Science and Technology (DISAT), Politecnico di Torino, Corso Duca degli Abruzzi, 10129 Turin, Italy

^bUniversité de Lyon, Institut de Chimie de Lyon, Laboratory of Chemistry, Catalysis, Polymers and Processes (C2P2, UMR 5265 - CNRS - University Claude Bernard Lyon 1 – Ecole Supérieure de Chimie Physique et Procédé CPE Lyon), Villeurbanne, France

*E-mail of corresponding author: simelys.hernandez@polito.it

Abstract

In this work, the synthesis of cheap BiVO₄ photoanodes for the photoelectrochemical water splitting reaction was optimized via the scalable thin film electrodeposition method. Factors affecting the photoelectrochemical activity, such as the electrodeposition time, the ratio of the Bi-KI to benzoquinone-EtOH in the deposition bath, and the calcination temperature, have been investigated by using the Central Composite Design of Experiments. Pristine monoclinic scheelite BiVO₄ photoanodes having a photocurrent density of $0.45 \pm 0.05 \text{ mA/cm}^2$ at 1.23 V vs RHE have been obtained. It was shown that a high photocurrent density is generally dictated by the following physico-chemical properties: a higher crystallite size, optimal thickness and a porous morphology, which give rise to a low charge transfer resistance, low onset potential and a high donor density. Moreover, to the best of our knowledge, this is the first report on the depth profile XPS analysis performed in BiVO₄ photoanodes made by electrodeposition technique, from which it was concluded that the surface V species exist as V⁴⁺ while the bulk V species are V⁵⁺. The V⁴⁺ induces a higher amount of surface oxygen vacancies, which was found to be beneficial for the photoactivity.

Keywords: BiVO₄ photoanode, water splitting, artificial photosynthesis, electrodeposition, XPS depth profile, Central Composite Design of Experiments.

1. Introduction

The conversion of solar energy to gaseous or liquid fuels provides an attractive pathway for energy storage and dispatch, which overcomes the inherent limitations associated with variable/seasonal availability and spatial nonuniformity of this renewable energy source. Photoelectrochemical (PEC) water splitting is a solar energy conversion process wherein photocatalytic materials use the photons coming from the sun to split water into H₂ (a sustainable fuel) and O₂, directly converting the solar energy into chemical energy. The bottleneck of this method is a 4-electron transfer process that happens at the photoanode during the water oxidation reaction: $2\text{H}_2\text{O} \rightarrow \text{O}_2 + 4\text{H}^+ + 4\text{e}^-$ [1,2] since stepwise one-electron transfers are necessary during the photochemically-activated reaction [3].

Several molecular catalysts [4] and inorganic catalysts [5] may be used to catalyse the water oxidation reaction via photo-assisted methods. Semiconductor metal oxides [6] that are composed of earth-abundant and non-noble metallic elements are preferred because of their proven stability under oxidizing conditions, low cost and sustainability. However, no single catalyst can fulfil all the requirements for an efficient water oxidation reaction. As frequently seen in literature, there are always trade-offs among the light-harvesting ability, the charge transport and charge transfer processes, and the catalyst's influence in the kinetics of the reaction.[7,8]

One interesting metal oxide that has drawn attention as a photoanode for the photoelectrochemical water splitting is bismuth vanadate (BiVO₄). The difference between its valence and conduction band edge positions is relatively low (2.4-2.5 eV) and they are positioned more strategically compared to those of the other metal oxides [9], therefore, it requires less bias potential and it is capable of accessing a wider portion of the solar spectrum. BiVO₄ has 3 main crystal forms: monoclinic scheelite, tetragonal zircon-type and tetragonal scheelite structure [10,11]. An irreversible transition from the tetragonal zircon-type to the monoclinic scheelite structure occurs at the calcination temperatures of 400 to 500°C. Meanwhile, a reversible transition between the monoclinic-scheelite to the tetragonal scheelite structures occurs at the temperature of 255°C, which gives its characteristic ferroelastic-paraelastic properties. Aside from the temperature-induced transitions, it was also reported that mechanical grinding at room temperature can irreversibly transform the tetragonal structure to the monoclinic structure [12] and the addition of Ag can progressively convert the monoclinic to tetragonal structures [13]. Among the three crystal structures of BiVO₄, monoclinic scheelite is the most commonly used structure in photocatalysis because of its higher photoactivity compared to the other structures [14]. Its theoretical maximum photocurrent density is 7.5 mA/cm². [15] If all of the photons possessing energies greater than 2.4 eV are absorbed, this translates to a 9% solar-to-hydrogen (STH) efficiency. [16] Moreover, it should be highlighted that the conduction band edge position of BiVO₄ almost coincides with the thermodynamic hydrogen evolution potential [11,17], which can contribute in the promotion of an earlier photocurrent onset and the generation of higher photocurrents in the low-bias region relative to the other photoanodes. [18] All of these factors are essential for the attainment of a high overall operating current that can lead to a high STH efficiency. [19] Lastly, BiVO₄ is known to be inexpensive and non-toxic. Similar to most metal oxides, it is stable against chemical and photoelectrochemical corrosion when coupled to appropriate co-catalysts or passivation layers. [20–22]

However, the use of BiVO₄ photoanodes entail several disadvantages. BiVO₄ is known to suffer from poor electron mobility, thus, photon efficiency is lost relatively easily due to electron-hole recombination. [23,24] This phenomenon is reportedly due to the disconnect among the VO₄ tetrahedra in the BiVO₄ structure, [25] which constrains the efficient flow of the photogenerated electrons towards the conducting support. In addition, in order to maximize the photogeneration of charges, the thickness of the material has to be optimized with respect to the optical penetration depth. [7,26] However, BiVO₄ has a short hole diffusion length that is estimated to be 70-100 nm, [27,28] which compromises and restricts the needed light penetration depth. In addition, BiVO₄ is known to exhibit poor water oxidation kinetics, which is a bottleneck that has to be overcome through co-catalyst deposition.

The properties and characteristics of the resulting BiVO₄ photoanode, or of the metal oxide semiconductors in general, largely depend on the synthesis method employed. There are several techniques that can be used to prepare the BiVO₄ photoanodes. One route is through the synthesis of the BiVO₄ powder via solid-state methods or solution-based techniques such as hydrothermal synthesis or sol-gel synthesis. An

extensive amount of literature covers the powder synthesis techniques that are employed in preparing BiVO₄ [29–32]. Then, the synthesized powders are deposited on the conductive electrodes via spin-coating, dip-coating or doctor-blade technique. These are simple techniques that can be easily implemented at cheaper cost. However, BiVO₄ powders that are synthesized by these methods usually suffer from very low surface area [19,33], typically of values less than 10 m²/g. The uniformity in the photoanode films produced by this method is also an issue for scaling up these methods. On the other hand, direct BiVO₄ thin films have been prepared by employing different deposition techniques. There are physical vapor deposition processes like molecular beam epitaxy and magnetron sputtering [34], which offer uniformity over large areas, a better control on stoichiometry, and ease of scalability [35], but may require some highly specialized and crystalline substrates as well as need high power and vacuum (at least 10⁻⁶ Pa) requirements, which might not be compatible with the more low-cost glass substrates that are normally used [7]. Chemical vapor deposition processes to deposit BiVO₄ offer highly crystalline and high quality thin films, with ample control on morphology via the control of the process conditions [36], but it uses relatively high temperature in order to evaporate the precursors. One of these techniques that are used to prepare BiVO₄ is atomic layer deposition [37], which is used to prepare highly controlled thin films that are deposited in a layer-by-layer, self-limiting manner, which finds huge advantage especially when the need to work with high-aspect ratio materials such as core-shell nanotube assemblies arise. The disadvantage of this process is it is slower relative to other techniques because it is performed in a layer-by-layer manner. Among the various thin film deposition techniques, the most promising in terms of scalability and ease of execution is electrodeposition. Although the technique is limited to the deposition of electrically-conductive materials, it is very much suited to the production of polycrystalline films of BiVO₄ with favorable porosity and well-developed nanostructures. Being a solution-based technique, the control of morphology can be accomplished by simply changing the different solution parameters while the thickness control can be accomplished by controlling the electrodeposition parameters, which are all done under ambient conditions, thus, relatively cheap and practical. However, the literature for electrodeposited BiVO₄ is not exhaustive. An interesting electrodeposition route for BiVO₄ synthesis has been developed by McDonald and Choi [19]. They developed an electrodeposition method for the synthesis of extremely thin 2D BiOI crystals via p-benzoquinone reduction. Because of its very thin structure (< 20 nm), the electrodeposited BiOI produced porous BiVO₄ photoanodes after mild chemical and thermal treatments. Further improvement into the process was introduced by Kim and Choi [38], who changed the vanadium precursor solution from V₂O₅/NH₄OH to VO(acac)₂/DMSO to improve the distribution of vanadium by improving the ease of wetting the electrodeposited BiOI surface. Despite its promise, the electrodeposition route of preparing BiVO₄ photoanodes is not well-studied, so it is a good method to explore.

In this paper, the synthesis, characterization, and the photoactivity of pristine BiVO₄ photoanodes that were synthesized via the electrodeposition of the Bi precursor and subsequent drop-casting of the V precursor have been studied. Starting from the original electrosynthesis recipe of Kim and Choi [32], an optimization experiment using the response surface methodology called the central composite design has been implemented. The effect of changing the different synthesis parameters (i.e. the electrodeposition time, the calcination temperature and the composition of the electrodeposition solution) to the resulting photocurrent density and material properties have been studied. A well-designed optimization study is necessary in order to gain results that are statistically valid, considering the design principles of randomization, replication and blocking. This can serve as a model for other optimization studies and demonstrate how a well-implemented response surface experimental design can be useful in this field. This is a strategy that is not often applied in the studies on photoelectrochemical water splitting. Most importantly, we have identified the most critical factors which significantly affect the behavior of the photocurrent density in the given synthesis procedure and described how each of these factors influence the performance of the synthesized catalysts. Finally, this paper reports a depth profile analysis of the prepared BiVO₄ photoanodes which has not been reported in literature to date. This new information confirms the role that oxygen vacancies on the catalyst surface play in the resulting photoactivity of the material.

2. Experimental

2.1 Materials

Bismuth (III) nitrate pentahydrate (Bi(NO₃)₃•5H₂O, ≥98%), vanadyl acetylacetonate (VO(acac)₂, ≥98%), potassium iodide (KI, ≥99%), p-benzoquinone (C₆H₄(=O)₂, ≥98%), absolute ethanol (CH₃CH₂OH, ETOH,

≥99.8%), dimethyl sulfoxide/DMSO (CH₃)₂SO, ≥99.9%), nitric acid (HNO₃, 70%) and sodium hydroxide (NaOH pellets, ≥97%), were utilized as-received from Sigma-Aldrich. Fluorine-doped tin oxide (FTO) conductive glasses with a sheet resistance of 7 Ω/cm² were obtained from Solaronix Inc. The FTO glasses were cleaned by sonication in acetone, ethanol and water, respectively, for 10 minutes each, prior to their use.

2.2 Investigation and optimization of BiVO₄ synthesis

The BiVO₄ synthesis procedure involves the electrodeposition of BiOI on FTO as the first step. The entire procedure is outlined in the supporting information section 2 (SI 2), which also shows the actual solutions and electrodes that were obtained. The electrodeposition solution was prepared by mixing 0.04 M of Bi(NO₃)₃•5H₂O that was dissolved in acidified 0.4 M KI aqueous solution (pH 1.7), with 0.23 M p-benzoquinone in absolute ethanol (Step 1).

Potentiostatic cathodic deposition was performed by using a 3-electrode assembly. An FTO glass served as the working electrode, a Ag/AgCl (3 M KCl) served as the reference electrode, and a Pt wire was used as the counter electrode to close the circuit. Different voltages (from -0.05V to -2V vs Ag/AgCl) and electrodeposition times (from 0.5min to 10 min) were investigated (Step 2). The geometric area was kept constant at 2 cm². The film thickness was obtained using a profilometer by tracing the surface topography of the samples.

After the deposition of BiOI, vanadium was introduced on the BiOI film by a dropwise addition of 180μL of a 0.2M vanadyl acetylacetonate solution. Two different solvents were investigated for the dissolution of the V-precursor: dimethyl sulfoxide (DMSO) and dimethyl fluoride (DMF).

In order to induce the formation of crystalline BiVO₄, the samples were calcined using different ramp rates, a slow rate (2°C/min) and a fast one (20°C/min), and at various temperatures from 350 to 500°C (Step 3). The calcined FTOs were then gently stirred in 1M NaOH solution for 30 minutes to dissolve the excess V₂O₅ (Step 4). Finally, pristine BiVO₄ electrodes were obtained after washing the electrodes with ultrapure H₂O.

Preliminary factor screening tests (details shown in the Supporting Information, SI, section SI-1) were performed in order to identify the factors that presented the most influence on the photoactivity. The effects of each identified factor (indicated in SI-3) and their different levels on the photoactivity have been thoroughly investigated. Furthermore, the identified factors (electrodeposition time, calcination temperature and Bi-KI to benzoquinone-EtOH ratio) were then optimized using the central composite design of experiments (CCDE) by utilizing the photocurrent density as the response variable. Each factor was varied across 5 levels in the experiment. The experimental runs have been performed in a randomized order, employing the design principles of replication, randomization and blocking. A 6-point replication of the centre points of the experimental design have been performed.

2.3 BiVO₄ thin film characterization

A Merlin Zeiss Field Emission – Scanning Electron Microscope (FE-SEM) that was equipped with an Energy Dispersive X-ray Spectroscopy System (EDS) was used to study the morphology of the samples.

The XRD spectra were obtained by using a Panalytical X'Pert PRO diffractometer under Cu Kα radiation (λ = 1.5418 Å) set at 40 kV and 40 mA, in order to determine the crystallinity of the BiVO₄ films. Crystallite sizes were calculated by using the Scherrer formula $D = k\lambda / \beta \cos \theta$, where D is the average crystallite size (nm), λ is the wavelength of the X-ray radiation (0.15418 nm), k is the shape factor (0.90) and β is the full-width half maximum, which was corrected for instrumental broadening. Calculations were done in the Panalytical High Score software by referencing the profile width of the samples to the LaB6 employed as a standard, whose pattern was collected in the same optical and acquisition conditions of the samples. The calculation was done after fitting a Pseudo-Voigt profile function into the measured data.

The UV-vis absorption spectra were obtained by using a Varian Cary 5000 spectrophotometer in the diffuse reflectance mode with an integrating sphere. The optical band gap energies were calculated by using the Tauc relation $\alpha hv = A(hv - E_g)^n$, where α is the absorption coefficient, A is a constant that is related to the mass of electrons and holes, E_g is the band gap energy, and the value of n depends on the type of transition ($n=1/2$ for allowed direct transition and 2 for allowed indirect transition). The majority of the literature suggests that BiVO_4 follows an allowed direct transition. In this work, the band gap of the BiVO_4 films was calculated by using the equation $\alpha hv^2 = A(hv - E_g)$, through a plot of αhv^2 vs hv , which has a linear region having a slope A and the extrapolation of $\alpha hv = 0$ gives the direct E_g . The band gap calculations using indirect band gap transition were similarly performed and the results obtained were almost equivalent to the direct band gap transition calculations.

The X-ray photoelectron spectroscopy (XPS) measurements were performed by using a PHI 5000 Versa probe instrument equipped with a monochromatic X-ray source of 1486.6 eV (Al $K\alpha$) in order to determine the surface composition of the prepared electrodes. High resolution (HR) analysis has been performed using a pass energy of 23 eV, with a double charge compensation made by Ar^+ and electron beam sources. The deconvolution procedure has been completed by using a Multipak 9.0 dedicated software. C 1s core level has been used and referenced at 284.5 eV. The Pseudo-Voigt function has been applied for curve-fitting the experimental data, while the Shirley function has been used to subtract the background signal.

2.4 Photoelectrochemical tests

A 3-electrode system with a Pt coil counter electrode (CE), Ag/AgCl (3M KCl) reference electrode (RE), and the prepared BiVO_4 photoanode as the working electrode (WE), were set up in a single-compartment quartz cell containing a 0.1 M phosphate buffer solution at pH 7. To simulate sunlight irradiation, a Newport 450 W Xe lamp with an AM 1.5G filter was employed, using an intensity of 100 mW/cm² for all the tests. The entire electrode geometric area of 2 cm² was illuminated.

PEC activity tests were performed by using a BioLogic VSP 300 potentiostat. In order to characterize the photocatalytic activity of the BiVO_4 photoanodes, linear sweep voltammetry (LSV) in continuous and chopped light modes, and chronoamperometry (CA), were employed. The LSV curves show the behaviour of the photocurrent density as a function of the applied potential in the PEC system, while the CA curves show the behaviour of the photocurrent density over time at a fixed voltage, which was 0.61 V vs Ag/AgCl (1.23 V vs RHE) in this case. Linear sweep voltammetry was performed at the potential range of -0.3 to 1 V vs. Ag/AgCl at a scan rate of 10 mV/s. Chronoamperometry was done at 0.61V vs. Ag/AgCl. For the conversion of the measured potentials versus the Ag/AgCl (3M KCl) reference electrode to RHE (NHE at pH=0), the following Nernst equation was used.

$$E_{RHE} = E_{\frac{Ag}{AgCl}} + 0.059pH + E_{\frac{Ag}{AgCl}}^0 \left(\frac{E_{\frac{Ag}{AgCl}}^0}{E_{\frac{Ag}{AgCl}}} = +0.199 V \right) \quad (1)$$

In order to examine the carrier mobility and the photocatalytic potential of the BiVO_4 films, staircase potentiostatic electrochemical impedance spectroscopy (SPEIS) was performed for each sample, using the potential range of -0.8 to 1 V (vs. Ag/AgCl), and a frequency of 7.5 kHz with an amplitude of 25 mV. Then, Mott-Schottky plots were drawn to extrapolate the flat band potentials (E_{fb}) and the donor densities (N_D) of the photoanodes, according to the equation (2):

$$\frac{1}{C^2} = \frac{2}{\epsilon\epsilon_0 A^2 e N_D} \left(E - E_{fb} - \frac{k_B T}{e} \right) \quad (2)$$

where C is the interfacial capacitance, ϵ is the dielectric constant of the semiconductor, ϵ_0 is the permittivity of free space, A is the area of the interfacial capacitance, N_D is the donor density, E is the applied potential, E_{fb} is the flat-band potential, k_B is the Boltzmann's constant, T is the temperature and e is the electronic charge. A plot of $\frac{1}{C^2} A^2$ versus the potential yields a linear region. From the value of this slope, the N_D of a semiconductor can be calculated and the intercept of the extrapolation of this linear plot to $\frac{1}{C^2} A^2 = 0$ gives its flat band

potential. A positive slope indicates that the material is an n-type semiconductor and electrons are the majority charge carriers.

Charge transport and transfer properties of the photoanodes were investigated using electrochemical impedance spectroscopy (EIS) measurements, in the frequencies ranging from 0.1 Hz to 0.5 MHz, at 0.61 V vs. Ag/AgCl, under simulated sunlight illumination (100 mW/cm²).

3 Results and Discussions

This section reports the findings about the optimization of the critical factors for BiVO₄ synthesis, describes the bulk and surface characteristics of these BiVO₄ photoanodes and then presents the effects of the said critical factors on the physico-chemical properties and the photoactivity of the photoanode.

3.1 Optimization results

Three-dimensional response surface plots were generated as shown in Fig. 1 to identify the ideal region of operability for this process. An initial factor screening scheme (see SI, section SI 1) was implemented to identify the critical factors that affect the response variable, i.e. the photocurrent density. The response surface methodology (RSM) then produced an empirical polynomial model based on the Taylor series to yield an approximation of the response surface over a region of factors, while also considering the interaction of these

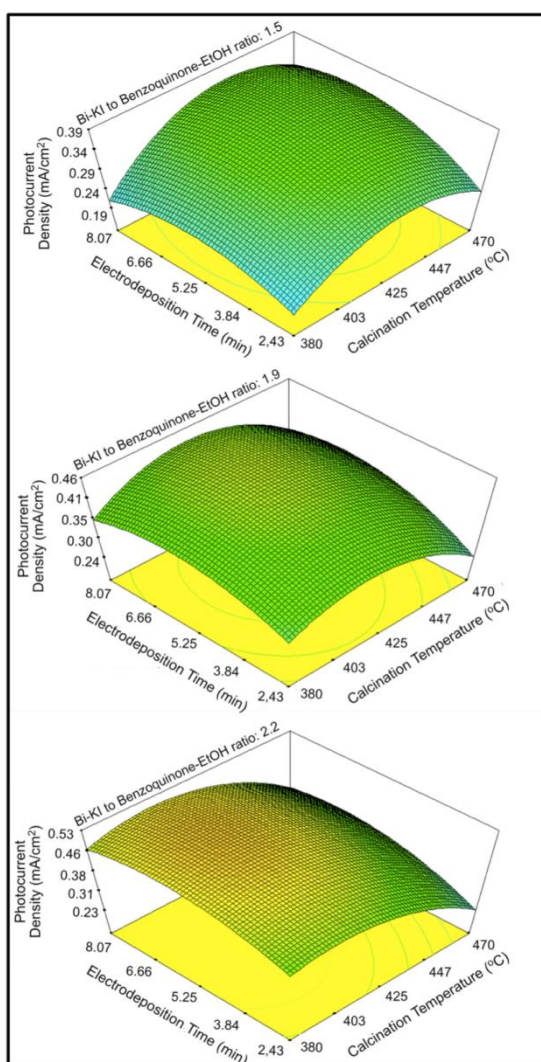


Fig. 1 - Response surface plots of optimization studies

factors. The response can change when the experiment is performed at a different value of the factors that were held constant, as a result of factor interactions, and this is captured by studying the response surface.

Considering the 6-point replication that was performed, an experimental value for the photocurrent density of 0.45 ± 0.05 mA/cm² at 1.23 V vs RHE was obtained for an electrodeposition time of 5.25 min, a calcination temperature of 425°C, and a Bi-KI to benzoquinone-EtOH ratio of 1.9. The optimization response surface plots in Fig. 1 indicate that an optimal photocurrent density of 0.53 mA/cm² at 1.23 V vs RHE can be obtained by changing the Bi-KI to benzoquinone-EtOH ratio to 2.2. Empirically, the resulting photocurrent densities for the Bi-KI to benzoquinone-EtOH ratios of 1.9 and 2.5 yielded similar photocurrent responses. Thus, the photocurrent density that were experimentally obtained at an electrodeposition time of 5.25 min, a calcination temperature of 425°C, and a Bi-KI to benzoquinone-EtOH ratio of 1.9 already lies within this optimal region of the response surface, and it is already indicative of the desired window of operability for the water oxidation reaction using the BiVO₄ photoanodes that were prepared in this study.

3.2 Bulk and surface characteristics of the BiVO₄ photoanodes

The synthesized photoanodes exhibited nanoporous structures as seen in the FE-SEM image shown in Fig.2A. In addition, the XRD spectra for the BiVO₄ photoanodes at different calcination temperatures, revealed that the monoclinic scheelite structure (JCPDS No. 14-0688, space group: I2/a, a=5.195, b=11.701, c=5.092, $\beta=90.38^\circ$) was obtained for these electrodes, which is evident from the peak splitting at the 18.5° and 35° of 2 θ (see arrows in Fig.2B). The FE-SEM images and XRD spectra of all the other synthesized samples under different parameters are shown in the SI (Sections SI 4, SI 5 and SI 6).

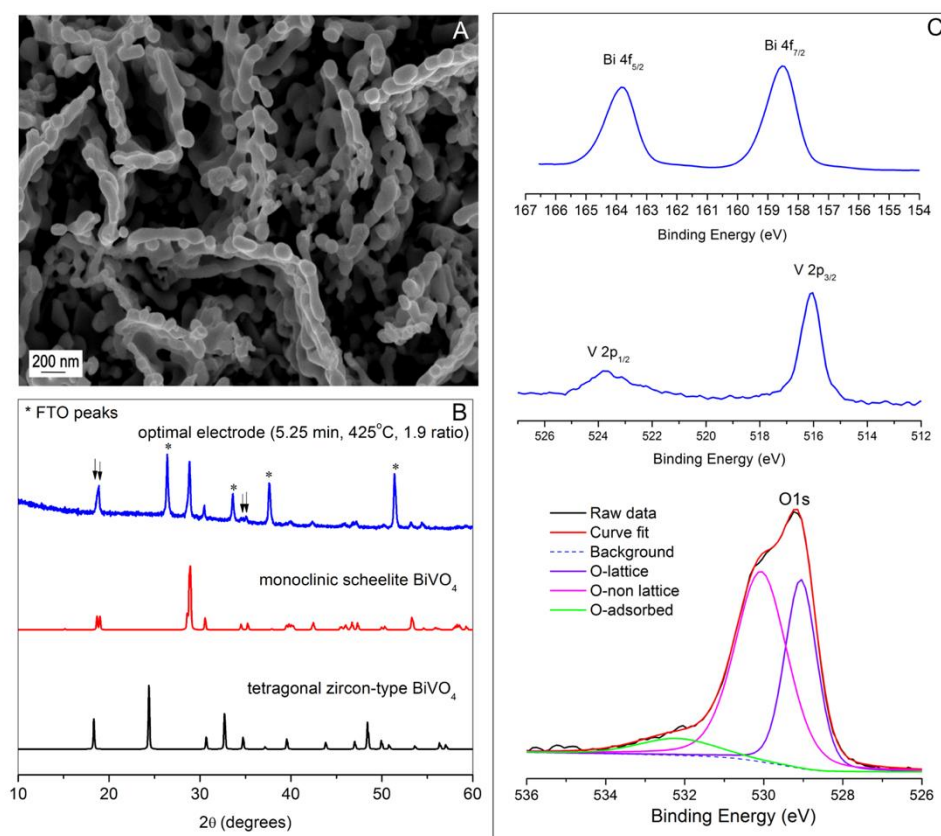


Fig.2 - (A) FE-SEM image, (B) XRD spectra and (C) Bi 4f, V 2p and O 1s XPS spectra of optimal BiVO₄ photoanode (5.25 mins, 425°C, 1.9 Bi-KI to benzoquinone-EtOH ratio).

The mean crystallite sizes (calculated from data on (011), (121) and (040) facets), and the ratio between the crystal facets (040) and (110) were calculated from the XRD data. The photocatalytic activity of BiVO₄ powders have previously been reported to be directly proportional to the exposure of the (040) facet, which is assumed to provide a multi-atomic BiV₄ centre that makes the electron transfer more facile [39–41]. Hence,

the normalized XRD intensity peak parameter, (040)/(110) ratio, was used to compare the XRD intensities, using the (110) peak considered as an internal standard. Moreover, optical band gap energies were calculated from the UV-vis diffuse reflectance spectra by using the Kubelka-Munk function and the Tauc relation for a direct band gap semiconductor, as it was done in previous literature reports, and in agreement with the behaviour of all the BiVO₄ thin films that were synthesized in this study. From these data, the band gap energy calculations yielded values ranging from 2.51 to 2.63 eV, signifying absorption in the visible light range. Please refer to the SI (Figure SI-12) for the plots showing the summary of the physico-chemical properties resulting from the variation of each synthesis parameter.

The high resolution XPS spectra for the Bi 4f, V_2p, and O_1s binding energy regions that were obtained for the optimal electrode are shown in Fig.2C. The XPS spectra for the other electrodes are shown in the SI (section SI 9). It is noteworthy that the Bi_4f_7/2 and Bi_4f_5/2 peaks appear in the binding energy region (158.5 eV and 163.8 eV, respectively) that is much higher than that of metallic Bi, *i.e.* 156.8 eV and 162.2 eV [42], respectively. These Bi 4f peaks indicate the presence of Bi occurring mainly as Bi³⁺ species in the surface of the electrodes. Meanwhile, the V_2p_3/2 and V_2p_1/2 peaks at 516.1 eV and 523.7 eV, respectively, are characteristic of V occurring as V⁴⁺ species on the surface of the photoanode. This is different from the bulk V species, which have a V⁵⁺ oxidation state. Rossell *et al* [43] have reported a pronounced surface reduction of Vanadium from V⁵⁺ to V⁴⁺ in a commercial monoclinic scheelite BiVO₄ powder, which was attributed to the presence of intrinsic surface defects in the form of oxygen vacancies that directly impact the electronic structure of monoclinic scheelite BiVO₄.

The same reduction of the V oxidation state from +5 to +4 has been observed in all of the electrodeposited BiVO₄ electrodes that were prepared in this study. However, it should be reiterated that the nature of the V_2p region of V in the BiVO₄ surface should be interpreted with extreme caution, considering the spread in the reported values in literature [44]. Some reported standard deviations can sometimes cause the binding energies to slightly overlap between V⁵⁺ and V⁴⁺. In order to be more certain about the nature of the V oxidation state in the BiVO₄ surface as well as in the bulk, a depth profile analysis using XPS was performed via Ar⁺ ion bombardment, the results of which are shown in **Error! Reference source not found.** To the best of our knowledge, this is the first report of the depth profile analysis of the V_2p region of V in BiVO₄. It can be clearly seen from the table inset in **Error! Reference source not found.** that the as-grown sample (0 s Ar⁺ bombardment) manifested the V⁴⁺ in the surface, as previously reported for all the samples. Similarly, the 6 s Ar⁺ bombardment also revealed the presence of the V⁴⁺ in the surface. However, at increasing depths, after 36 s and 96 s of Ar⁺ bombardment, the peak shifted towards the V⁵⁺ region and the V³⁺ species started to appear. The appearance of the V⁵⁺ at higher depths confirms that the Ar⁺ bombardment removed the V⁴⁺ surface layer, which confirms that the bulk indeed consists of V⁵⁺, while the unexpected appearance of V³⁺ and V⁴⁺ at higher depths is attributed to the reduction of the V⁵⁺ that was induced by the Ar⁺ bombardment. This has been reported in a study by Silversmit *et al* [45] where Ar⁺ was found to have induced the reduction of V⁵⁺ to V³⁺ in the following manner: V⁵⁺ decreases fast and disappears within the first 30 s of Ar⁺ bombardment, after which the V⁴⁺ increases and reaches a maximum at 24 – 40s, and the V³⁺ build up from 30 s onwards. Thus, in summary, the surface V species have the V⁴⁺ oxidation state, while the bulk species contains V⁵⁺.

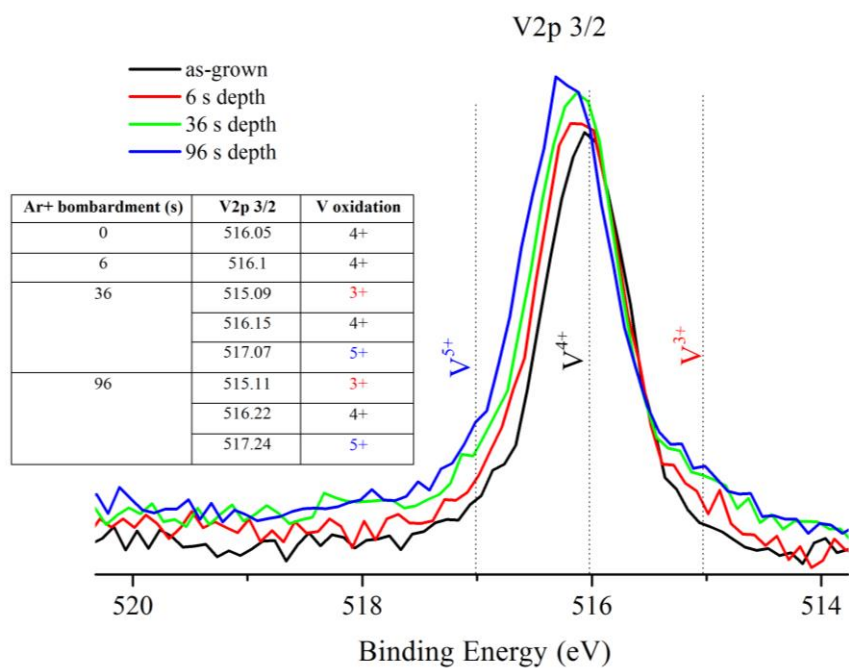


Fig 3. V_{2p} region of the depth profile analysis of the optimal electrode (5.25 min electrodeposition time, 425°C calcination temperature, 1.9 Bi-KI to benzoquinone-EtOH ratio).

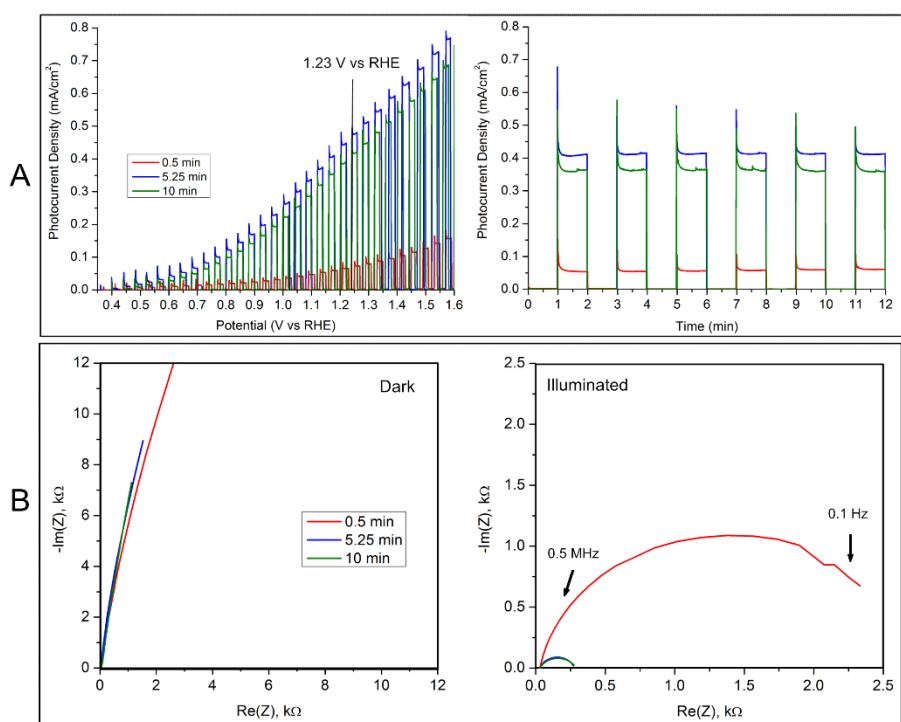


Fig 4. Photoelectrochemical characterization of samples at various electrodeposition time. (A) linear sweep voltammograms (scan rate: 10 mV/s) and chronoamperometry plots (potential: 1.23 V vs RHE), (B) Nyquist plots under dark and illuminated conditions. (0.1 M Na-Pi buffer pH 7).

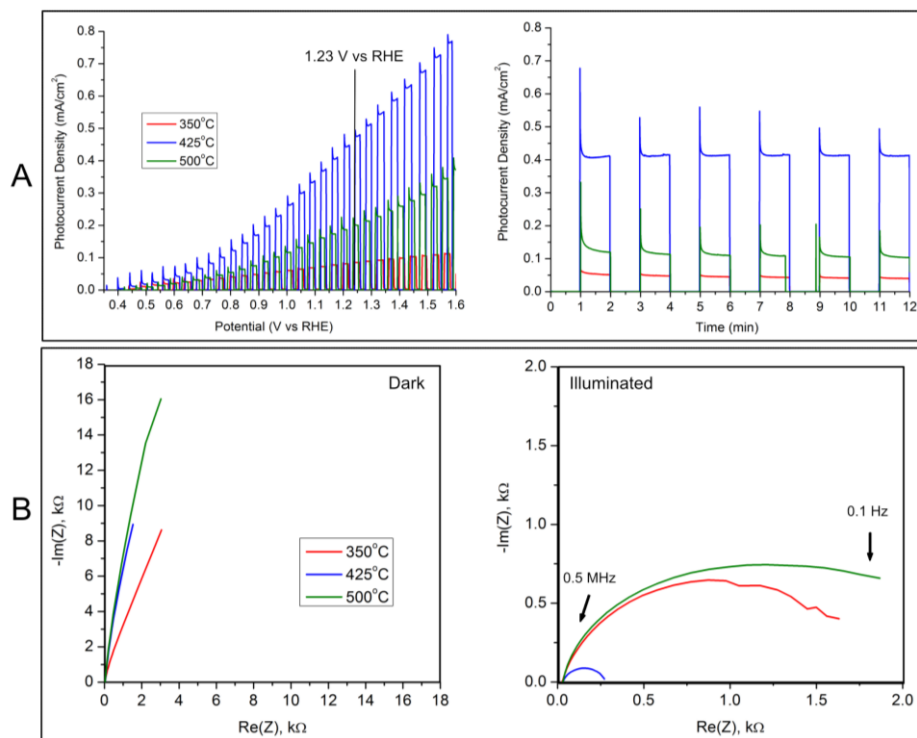


Fig. 5. _ Photoelectrochemical characterization of samples at various calcination temperatures. (A) linear sweep voltammograms (scan rate: 10 mV/s) and chronoamperometry plots (potential: 1.23 V vs RHE), (B) Nyquist plots of EIS measurements under dark and illuminated conditions. (0.1 M Na-Pi buffer pH 7).

Meanwhile, a deconvolution procedure that was applied to the O_1s spectrum as shown in Fig.2C reveals that the O species are divided into the following: oxygen due to the lattice structure, the non-lattice oxygen, and oxygen due to adsorbed molecules [42,46]. The deconvoluted O_1s peak at 529.2 eV is assigned to the oxygen in a BiVO₄ lattice environment, while the peaks at 530.3 eV and 532.0 eV are assigned to the non-lattice and adsorbed oxygen species, respectively [47,48,49]. Non-lattice oxygen refers to the oxygen-deficient regions, which might be populated with OH groups in order to correct the charge balance. Finally, the O_1s peak at 532.0 eV refer to the chemisorbed or dissociated oxygen from the water molecules. A proper amount of oxygen vacancies can aid in both bulk and surface charge separation [50] because the creation of oxygen vacancies brings about free electrons, which are shallow electron donors [46] that enhance the conductivity of the semiconductor. They also enhance the interfacial charge transfer by increasing the active sites, i.e. turning the V site into an active site, and by lowering the adsorption energies of some intermediates like H₂O_{ads}, OH_{ads}, and O_{ads}, thereby promoting an easier charge transfer to the electrolyte and improving the surface catalysis [50]. Also, oxygen vacancies facilitate hole trapping and migration and drive highly oxidizing hole migration at the semiconductor/electrolyte interface [51]. On the other hand, an excessive amount of the oxygen vacancies is detrimental to the photoactivity because the V⁴⁺ is characterized by a larger ionic radius than the V⁵⁺, and when they exist in excessive amounts, this can result to lattice distortion that can subsequently reduce the hole diffusion length [52].

The surface Bi/V atomic ratios that were measured using XPS and the bulk Bi/V atomic ratios that were obtained using EDS are reported in the SI (Figure SI-14). The bulk Bi/V ratios are consistently about 1, confirming the 1:1 ratio of the Bi:V atoms of BiVO₄, which is also confirms the presence of the V⁵⁺ species in the bulk. However, when the surface species of Bi/V are examined, it can be seen that the Bi concentration tends to be higher than that of the V atoms for all the synthesized electrodes. We have found that the Bi/V ratio for an untested electrode deposited at 5.25 minutes, 425°C and 1.9 Bi-KI to benzoquinone-EtOH ratio, results to a surface Bi/V of 2.3. This Bi-rich surface, consistent with the findings of Sayama *et al* [53], could have been due to the segregation phenomenon that has been observed for different Bi-containing oxides. The

depletion of O in the subsurface happens because of the segregation of O to the surface, which leads to Bi-O surface terminations as reported by Passerone *et al* [54]. This Bi-rich surface can either enhance the photoactivity by serving as a protective layer or be detrimental to it by worsening the catalytic activity of the BiVO₄ as a water oxidation catalyst [43]. This Bi/V ratio increases to 2.96 after the photoelectrochemical tests, while that for the bulk Bi/V remains unchanged at about 1. Thus, there was also a dissolution of surface V atoms from the BiVO₄ surface during the photoelectrochemical tests, which might have been due to the higher solubility of Vanadium over Bismuth under these conditions [55].

3.3 Effects of synthesis parameters on the physico-chemical properties and photoactivity

3.3.1 Electrodeposition time

Effect on physico-chemical properties

Increasing film thicknesses were obtained by using different electrodeposition times of 0.5, 5.25 and 10 minutes and the film thicknesses, measured by using a profilometer, were 56, 478 and 517 nm, respectively. A calcination temperature of 425°C and a Bi-KI to benzoquinone ratio of 1.9 were kept constant for all of these electrodes. The 0.5 min electrode did not completely cover the FTO surface, whose crystals are evident in the FE-SEM image shown in the Figure SI-8. However, after 5.25 min of electrodeposition, the FTO substrate was fully covered and a nanoporous BiVO₄ structure was produced, which tends to maintain the nanoflake structure of the electrodeposited BiOI material (refer to Figures SI-8 and SI-9), as the electrodeposition time increases and as the film thickness grows.

The XRD patterns (Figure SI-10A) showed that the thicker photoanodes exhibited the monoclinic scheelite structure while the thinnest electrode yielded an XRD spectrum similar to the FTO, which suggests that a very thin layer of BiVO₄ was deposited on the FTO surface for this sample. In agreement with the thickness measurements, the XRD peak intensities generated for the thickest film, *i.e.* 10 minutes of electrodeposition time, are generally higher compared to the other samples, which confirms that more material has been deposited on this FTO surface. This is seen most distinctively in the 2 θ peak of 29°. The mean crystallite size was the highest for the 5.25 min electrode (112 nm) and the lowest for the 0.5 min electrode (53 nm). In addition, the 0.5 min electrode had a negligible (040) peak and, therefore, almost zero value of the (040)/(110) ratio. A preferential growth of the BiVO₄ crystals along the (040) direction was observed by increasing the electrodeposition time, which should be beneficial for the photocatalytic activity of the film [39–41].

As reported in the Figure SI-12, the band gap energy of the sample electrodeposited for 0.5 min (2.63 eV) is higher than those of the samples prepared during 5.25 and 10 min of electrodeposition time, which have almost equal band gap energies, *i.e.* 2.55 and 2.56 eV, respectively, which are characteristic of the monoclinic scheelite BiVO₄ [56]. The higher band gap energy for the thinnest electrode was due to the contribution from the FTO that has a band gap energy of about 3.3 eV [57].

A slight shift of the binding energy for the O1s peak of the thinnest electrode (0.5 min) relative to the 5.25 and 10 min samples was observed (see Figure SI-13), which is due to the contribution of the oxygen vacancies in the exposed FTO, where F doping tends to substitute the O, which provides a free electron that serves as the reason for the dominant defects on FTO. As explained above for the optimum BiVO₄ film, the thicker BiVO₄ samples (5.25 and 10 min) clearly evidenced the presence of lattice oxygen and oxygen vacancies, the latter being the highest for the 5.25 min electrode. On the other hand, from the surface composition analysis that is shown in the SI (Figure SI-14), the 5.25 min sample has the lowest surface Bi/V ratio (2.96), while the 0.5 min sample has the highest surface Bi/V ratio (4.79) after testing.

Effect on photoelectrochemical properties

Error! Reference source not found.A reports the LSV curves for the samples that were electrodeposited at different times, which were acquired by using chopped light measurements. They show evidences of fast recombination of the photogenerated electron-hole pairs at the BiVO₄ surface, characterized by the

instantaneous dampening of the photocurrent density signal right after the light is turned on. The same is also evident in the CA plots displayed in **Error! Reference source not found.A**. This behaviour is typical of BiVO₄ electrodes without any co-catalyst on its surface that is able to enhance the kinetics of the water oxidation reaction [38]. From these plots, relatively stable mean photocurrent density values were obtained over the course of the measurement time of 12 minutes. The highest photocurrent density was obtained for the electrode that was electrodeposited for 5.25 minutes, that is 0.45 mA/cm² at 1.23 V vs. RHE (blue line). The least photocurrent density was for the 0.5 min sample (red line) having a photocurrent density of 0.06 mA/cm² at 1.23 V vs. RHE, while the 10 min sample generated a photocurrent density of 0.39 mA/cm² at 1.23 V vs. RHE (green line). By comparing the physico-chemical properties of these electrodes, it can be inferred that the best photocurrent density of the 5.25 min sample is related to its higher crystallite size (112 nm), optimal electrode thickness (478 nm) and lower surface Bi/V ratio.

A higher crystallite size is correlated also to a higher crystallinity, which together with the highest interconnection among the crystals and a more closed porosity of the 5.25 min sample, could have played a role in enhancing the carrier mobility in this electrode compared to the others. To confirm this hypothesis, the Mott-Schottky plots were recorded and analysed for these samples (Figure SI-15). These plots demonstrated the n-type behaviour of the BiVO₄ samples, as manifested by the positive slope of the linear data, and the mobility of the majority carriers was calculated. As expected, the donor density increased from the 0.5 min ($N_D = 2.35 \times 10^{19} \text{ cm}^{-3}$) to the 5.25 min ($N_D = 4.66 \times 10^{19} \text{ cm}^{-3}$) but then decreased at 10 min ($N_D = 3.00 \times 10^{19} \text{ cm}^{-3}$) of electrodeposition time. As mentioned previously, the highest presence of oxygen vacancies in the 5.25 min sample introduces shallow electron donors that additionally could aid in increasing the donor density in the semiconductor. The higher N_D of this sample could have played a role in improving the photoelectrochemical response due to two main reasons [17]. First, it raises the Fermi level, which increases the band bending in the space-charge region because of the bigger difference between the Fermi level and the redox potential of the electrolyte. Because of the increased band bending, the electric field in the space charge layer is similarly enhanced, which reduces the electron-hole recombination. Second, it enhances the electrical conductivity of the photoanode, thus, it improves the charge transport properties within the material.

Furthermore, there is an optimum thickness of BiVO₄ that was electrodeposited in the electrode after 5.25 min, which is higher in the present case (about 478 nm) than the optimum value of 200 nm that was previously reported for the BiVO₄ electrodes that were prepared by other techniques such as dip-coating. [40] This behaviour could be explained by the higher porosity and active surface that were available in the electrodeposited samples relative to the BiVO₄ films prepared by other techniques. Electrochemical impedance spectroscopy (EIS) is a powerful technique that was used to gain insights about the charge transfer rate due to the photoelectrochemical reaction, which is generally associated with the charge transfer resistance (R_{ct}), at the electrode-electrolyte interface. [58] The EIS results in this study are reported by using Nyquist plots, herein characterized by a single arc, whose diameter is proportional to the R_{ct} . This was further verified by using an equivalent circuit model (shown in the Figure SI-17), which was used to calculate the charge transfer resistances. The symmetric Nyquist plots in both the dark and illuminated conditions are shown in **Error! Reference source not found.B**. The thinnest and worst-performing electrode (0.5 min sample) had the highest charge transfer resistance (2.7 k Ω), while the corresponding charge transfer resistances for the 5.25 min and 10 min samples are much smaller and practically equal (0.25 and 0.26 k Ω , respectively). This explains the higher photocurrent density of the 5.25 and 10 min samples in comparison to the 0.5 min electrode.

A further increase in the electrode thickness of 39 nm by electrodeposition for 10 min has caused a reduction of 13% in the photocurrent density. It is possible that this accompanying increase in thickness has contributed to more defect levels that could have acted as charge recombination sites. Indeed, the lower surface Bi/V ratio of the 5.25 min sample is favourable because this leads to a lower presence of the Bi-O surface terminations that have a poorer photocatalytic activity for the water oxidation, which could have contributed to the lower activity of the 10 min sample that has a higher Bi/V ratio. These results are also in agreement with the determined onset potentials of these electrodes: 0.36, and 0.40 V vs RHE for the 5.25 min and 10 min samples, respectively, taken from a magnified region of interest in the LSV plots (Figure SI 16). The 5.25 min sample has the least onset potential, which is another indicator of its superior catalytic activity. A low onset potential is important because it gives way to a practical implementation of the device to be achieved at a lower bias.

In conclusion, the highest photocurrent density of the 5.25 min sample can be attributed to the following photoelectrochemical characteristics: lowest charge transfer resistance, highest donor density, and lowest onset potential, which highly depends on physico-chemical properties like higher crystallite size, optimal electrode thickness, and a lower surface Bi/V ratio.

3.3.2 Calcination temperature

Effect on physico-chemical properties

The effect of the calcination temperature was investigated at 350, 425 and 500°C, at an electrodeposition time of 5.25 min and a Bi-KI to benzoquinone-EtOH ratio of 1.9. There were pronounced differences in the morphology of the samples that were calcined at different temperatures, as shown in Figure SI-8. All the BiVO₄ films possess a nanoporous structure, but the pores decreased in size as the crystals grew. The 350°C sample showed the formation of small crystals that are agglomerated in a network that follows the shape of the pristine BiOI nanoflakes (see section SI 5), which seem to stick to one another. As the temperature increased, the small crystals sintered together into larger crystals, achieving up to about 200 nm of length and formed the interconnected globules, which are visible in the FESEM images of the samples calcined at 500°C.

XRD data in Figure SI-10B shows that the three BiVO₄ samples calcined at 350, 425 and 500°C clearly exhibited the monoclinic scheelite structure. The presence of the tetragonal zircon-type phase that could be present in the samples calcined at 350°C can be excluded due to the absence of the main peaks at 24.3° and 32.7° that are associated with this crystalline structure. The peak splitting of the characteristic peaks that were observed at 18.5° and 35° of 2θ was more pronounced as the calcination temperature increased, which is most likely due to an increase in the crystallinity of the monoclinic scheelite phase in the BiVO₄ samples because the thicknesses of these electrodes are similar. Indeed, in agreement with the FESEM images, the mean crystallite sizes that were calculated from the XRD data also increased by increasing the calcination temperature. However, the peak related to the (040) facet was absent in the sample calcined at 350°C, most probably due to the small size of the crystals (*i.e.* 22 nm and 13 nm for the (011) and (121) facets, respectively). Meanwhile, by increasing the temperature, the samples grew along all directions. It is noteworthy that the electrodes calcined at 425 and 500°C have an almost similar mean crystal size of 112 and 115 nm, respectively, while having almost the same ratios of the (040)/(110) facets, that are 0.52 and 0.49, respectively, as shown in Figure SI-12.

The band gap energies that were obtained for these samples did not vary significantly and ranged from 2.51 to 2.55 eV, with a very slight advantage towards the 350°C electrode, because of its slightly lower band gap energy value. These values are slightly higher than the generally reported values of 2.4 eV for BiVO₄. [56]

Based on the XPS spectra (Figure SI-13), the Bi species are mainly Bi³⁺ and the V species are occurring mainly as V⁴⁺. From the O1s region, it can be seen that the sample 425°C has the highest amount of oxygen vacancies among all the samples. Moreover, as reported in **Figure B**, the surface Bi/V ratios were almost equal for the 350 (2.92) and 425°C (2.96) samples, while it was significantly higher for the 500°C sample (3.65).

Effect on photoelectrochemical properties

The photoelectrochemical results (LSV plot) of the samples that were calcined at different temperatures are reported in the **Error! Reference source not found.A**. The least photocurrent density was obtained for the 350°C sample (red line), which generated a very low photocurrent of 0.08 mA/cm² at 1.23 V vs. RHE, which can be attributed to the low crystallinity of this sample. The 500°C sample (green line) demonstrated a photocurrent density of 0.19 mA/cm² at 1.23 V vs. RHE, which was 58% higher than that of the 350°C sample, but only 42% of the maximum value that was achieved by the sample calcined at 425°C (blue line). Since the crystallinity, crystallites size, band gap energy and (040)/(110) ratio for these two last samples are almost the same, the main parameters that could play a role on their different activity are their thickness and morphology. The electrode needs to be thick enough to enhance the absorption of the photons but at the same time, it needs to be thin enough to avoid the formation of defect levels that can act as charge recombination sites. A perfect compromise between these two properties is the ideal condition.

As explained previously, the physico-chemical properties have an influence on the photoelectrochemical behaviour and they caused the highest photocurrent density of the 425°C sample due to the following characteristics: least charge transfer resistance, highest donor density, and the lowest onset potential. Indeed, as shown in the Nyquist plots in **Error! Reference source not found.B**, this photoanode (425°C sample, blue line) have the lowest R_{ct} (0.25 k Ω) under illumination conditions (see also Figure SI-17). Meanwhile, the R_{ct} of the 350°C sample (red line, 2.2 k Ω) and the 500°C sample (green line, 1.8 k Ω) are significantly higher than the former. The EIS data indicates a superior reaction kinetics and photoelectroactive surface at the electrode-electrolyte interphase on the electrode that was calcined at 450°C, which is also confirmed by the lower onset potential of this sample (0.36 V vs RHE) than for the 350°C and 500°C samples (having an onset of 0.44 V and 0.38 V vs RHE, respectively). The donor density values (see Figure SI-15) were found to increase from $3.39 \times 10^{19} \text{ cm}^{-3}$ to $4.66 \times 10^{19} \text{ cm}^{-3}$ when the calcination temperature was increased from 350 to 425°C, and then decreased to $3.82 \times 10^{19} \text{ cm}^{-3}$ in the 500°C sample. This can be explained by the XRD and FESEM results: the lower calcination temperature (350°C) induces a lower crystallinity that reduces the e^- mobility and the further growth of BiVO₄ crystals at the highest temperature could cause less interconnected surface of the BiVO₄ crystals, and the exposure of free FTO substrate, which could possibly induce a lower rate of electron flow and collection, and a higher rate of charge (e^-/h^+) recombination in the 500°C sample than in the 425°C electrode.

On the other hand, despite having a slightly higher charge transfer resistance and a lower thickness, the 500°C sample exhibited a higher photocurrent density than the 350°C sample, mainly because of its lower onset potential, higher donor density, and the prevalence of the (040) facet, as explained above.

3.3.3 Bi-KI to Benzoquinone-Ethanol Ratio

Effect on physico-chemical properties

The effect of varying the Bi-KI to benzoquinone-ethanol ratio was also investigated by using the ratios of 1.3, 1.9, and 2.5, at a calcination temperature of 425°C and an electrodeposition time of 5.25 min. As seen in the FESEM images in Figure SI-8, this parameter significantly affected the morphology of the synthesized BiVO₄ thin films. Although all the samples that were synthesized at these conditions yielded nanoporous structures, the globules formed at the ratio of 1.3 exhibited a high agglomeration and closure of most of the porosity. The samples 1.9 and 2.5 ratios have morphologies that are quite similar, both showing a higher degree of porosity than the one prepared with a ratio of 1.3. All these samples possessed the monoclinic scheelite structure (Figure SI-10C). As expected, depending mostly on the deposition time, the electrodes thickness was similar for the 1.9 and 2.5 ratio samples (i.e. 478 nm, and 457 nm, respectively), while for the 1.3 ratio the thickness was lower indicating that 1.9 is close to the minimum value for this parameter to guarantee an optimum BiVO₄ yield. Indeed, as shown in the Figure SI-12, the highest crystallite size was obtained for the 1.9 ratio sample (112 nm), while the lowest one was obtained for the 1.3 ratio sample. The 1.9 sample also exhibited the highest (040)/(110) facet ratio and the lowest surface Bi/V ratios (Figure SI-13) of 2.96, which are characteristics that could play in favour of the photoactivity of this sample.

There were no significant differences in the photon absorption capacity for these samples since their band gap energy values did not vary significantly (ranged between 2.53 to 2.56 eV, Figure SI-11C and SI-12). From the XPS analyses (Figure SI-13, all the Bi species are mainly Bi³⁺, and the V species are occurring mainly as V⁴⁺ and the O1s deconvolution spectra showed that the amount of oxygen vacancies were quite comparable for these three samples.

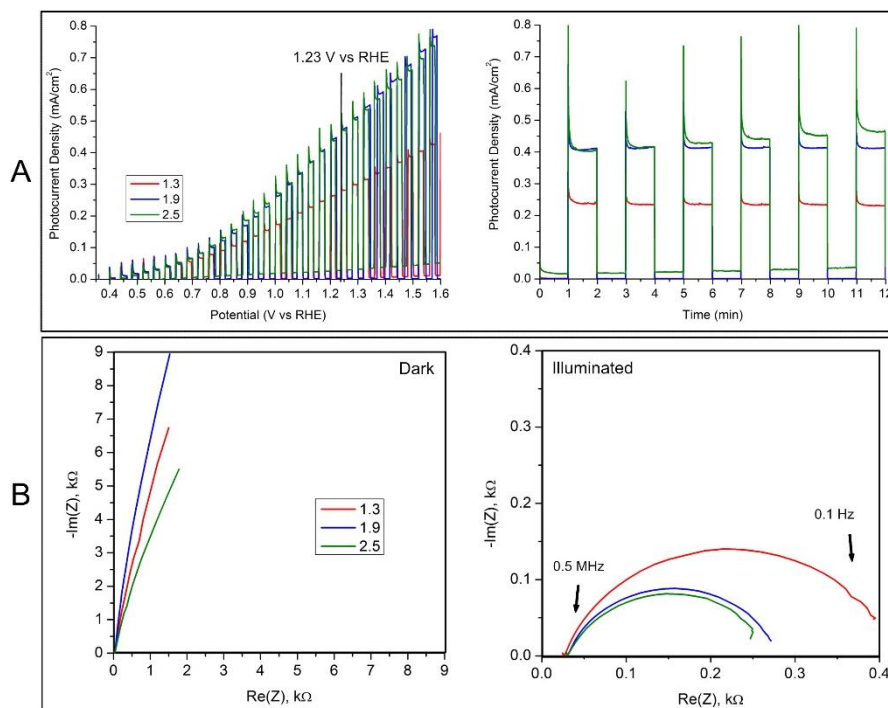


Fig. 6. _ Photoelectrochemical characterization of samples at various Bi-KI to benzoquinone-EtOH ratios. (A) linear sweep voltammograms (scan rate: 10 mV/s) and chronoamperometry plots (potential: 1.23 V vs RHE), (B) Nyquist plots of EIS measurements under dark and illuminated conditions. (0.1 M Na-Pi buffer pH 7)

Effect on photoelectrochemical properties

Among the calcined samples that were made with different Bi-KI to benzoquinone-EtOH ratios, the least photocurrent density was observed for the 1.3 ratio sample (0.29 mA/cm^2 at 1.23 V vs. RHE), as reported in Fig. 6A (see also Figure SI-12). The photocurrent density for the 1.9 and 2.5 ratio samples were about 36% higher than the 1.3 electrode, but they achieved almost similar photoactivities: 0.45 mA/cm^2 and 0.43 mA/cm^2 at 1.23 V vs RHE, respectively. The onset potential (Figure SI-16) was equal for both the 1.9 ratio and 2.5 ratio (0.36 V vs RHE), while it was higher for the 1.3 ratio (0.4 V vs RHE). The lowest activity of the 1.3 sample can be explained by its lower thickness, while the other two electrodes possess almost similar morphologies, thicknesses, and band gap energies. Thus, the very slight advantage of the 1.9 ratio electrode lies in the higher crystallite size, higher (040)/(110) ratio, and lower surface Bi/V ratio compared to the 2.5 ratio electrode.

These results are in agreement with the Nyquist plots of the EIS measurements under illumination shown in Fig. 6B. The worst-performing electrode with a 1.3 ratio (red line) have the highest R_{ct} ($0.39 \text{ k}\Omega$), while the 2.5 ratio sample (green line, $0.24 \text{ k}\Omega$) and the 1.9 ratio sample (blue line, $0.25 \text{ k}\Omega$) showed almost similar R_{ct} values, indicating an enhanced electroactive surface area that is available for the photocatalytic reaction on these latter samples, which also have an improved porosity with respect to the 1.3 electrode. Moreover, the donor density value (Figure SI-15) for the 1.9 ratio sample was the highest ($4.66 \times 10^{19} \text{ cm}^{-3}$), indicating its superior electron mobility. This value is followed by the 2.5 ratio ($4.1 \times 10^{19} \text{ cm}^{-3}$), while the 1.3 ratio has the least donor density ($3.46 \times 10^{19} \text{ cm}^{-3}$), which can be related to a poorer e^- mobility due to a poorer interconnection among the BiVO_4 nanoparticles that were formed under this electrodeposition condition.

To summarize, the optimization of the BiVO_4 photoanode synthesis revealed that a 5.25-minute electrodeposition time using an electrodeposition solution consisting of a 1.9 Bi-KI to benzoquinone-EtOH ratio and a calcination temperature of 425°C yields an optimal photocurrent density of $0.45 \pm 0.05 \text{ mA/cm}^2$ at 1.23 V vs RHE. This nanoporous electrode exhibited the monoclinic scheelite structure, with surface V^{4+}

species that signify the presence of oxygen vacancies in the surface and bulk V^{5+} species. The presence of a higher amount of oxygen vacancies has been shown to be beneficial to the photoactivity of the electrode as well as high crystallite size, an optimal thickness and a porous morphology. These factors contribute to the low charge transfer resistance, low onset potential and a high donor density for this electrode that ultimately yielded favourable photocurrents.

4 Conclusion

In this work, the optimization of the BiVO_4 photoanode preparation via thin film electrodeposition on FTO was performed. Factors affecting the photoelectrochemical activity such as the electrodeposition time, the ratio of the bismuth precursor to the reduced reagent in the deposition bath, and the calcination temperature, have been investigated by using the Central Composite Design of Experiments. Pristine monoclinic scheelite BiVO_4 photoanodes having a photocurrent density of $0.45 \pm 0.05 \text{ mA/cm}^2$ at 1.23 V vs RHE have been obtained. It was shown that a high photocurrent density is generally dictated by the following physico-chemical properties: a higher crystallite size, an optimal thickness and a porous morphology, which give rise to a low charge transfer resistance, low onset potential and a high donor density. The optimization of the critical synthesis factors sheds light on the proper design and fabrication of efficient bare BiVO_4 photoanodes for solar fuels production, whose efficiency can be further improved by the deposition of O_2 evolution co-catalysts to reduce the superficial e^-/h^+ recombination.

To the best of our knowledge, this is the first report on the depth profile analysis that was performed on the V2p spectra of V in the optimized BiVO_4 electrodes, from which it was concluded that, as a result of the electrodeposition technique that was employed, the surface V species exist as V^{4+} , while the bulk V species are V^{5+} . The V^{4+} induces a higher amount of surface oxygen vacancies, which was found to be beneficial for the photoactivity. Optimizing the amount of superficial oxygen vacancies and finding a way to stabilize them could be a new strategy to further improve the photoactivity of BiVO_4 photoanodes.

Acknowledgments

The authors thank the EACEA Erasmus+ _SINCHEM Grant FPA 2013-0037 for the financial support. Flavia Calignano and Mauro Raimondo are acknowledged for the film thickness and FE-SEM/EDS measurements, respectively.

References

- (1) Hurst, J. K. Catalysts for Solar Fuel Production. *Science* **2010**, 328 (April 1 J. K. Hurst, *Science* (80-.), 2010, 328, 315–316.), 315–316. <https://doi.org/10.1126/science.1187721>.
- (2) Grätzel, M.; Moser, J. Solar Energy Conversion. **2001**, 5, 589–644.
- (3) Inoue, H.; Shimada, T.; Kou, Y.; Nabetani, Y.; Masui, D.; Takagi, S.; Tachibana, H. The Water Oxidation Bottleneck in Artificial Photosynthesis: How Can We Get through It? An Alternative Route Involving a Two-Electron Process. *ChemSusChem* **2011**, 4 (2), 173–179. <https://doi.org/10.1002/cssc.201000385>.
- (4) Wang, M.; Artero, V.; Hammarstr, L.; Martinez, J.; Karlsson, J.; Gust, D.; Summers, P.; Machan, C.; Bruggeller, P.; Windle, C. D.; et al. Molecular Catalysts for Artificial Photosynthesis: General Discussion. **2017**, 353–395. <https://doi.org/10.1039/C7FD90017A>.
- (5) Kumagai, H.; Hammarstr, L.; Whang, D. R.; Shinohara, Y.; Martinez, J.; Karlsson, J.; Summers, P.; Windle, C. D.; Kodera, M.; Cogdell, R.; et al. Inorganic Assembly Catalysts for Artificial Photosynthesis: General Discussion. **2017**, 481–507. <https://doi.org/10.1039/C7FD90018J>.
- (6) Fujishima, A.; Honda, K. Electrochemical Photolysis of Water at a Semiconductor Electrode. *Nature* **1972**, 238 (5358), 37–38. <https://doi.org/10.1038/238037a0>.
- (7) Chen, Z.; Dinh, H. N.; Miller, E. *Photoelectrochemical Water Splitting*; 2013. <https://doi.org/10.1007/978-1-4614-8298-7>.
- (8) Walter, M. G.; Warren, E. L.; McKone, J. R.; Boettcher, S. W.; Mi, Q.; Santori, E. A.; Lewis, N. S. Solar Water Splitting Cells. *Chemical Reviews (Washington, DC, United States)* **2010**, 110 (11), 6446–

6473. <https://doi.org/10.1021/cr1002326>.

- (9) Tolod, K. R.; Hernandez, S.; Quadrelli, E. A.; Russo, N. Chapter 4: Visible Light-Driven Catalysts for Water Oxidation: Towards Solar Fuel Biorefineries, in *Horizons in Sustainable Industrial Chemistry and Catalysis*, Editors: S. Albonetti, S. Perathoner, and E.A. Quadrelli. Elsevier 2019. DOI: <https://doi.org/10.1016/B978-0-444-64127-4.00004-5>.
- (10) Lim, A. R.; Choh, S. H.; Jang, M. S. Prominent Ferroelastic Domain Walls in BiVO₄ Crystal. *Journal of Physics: Condensed Matter* **1995**, *7* (37), 7309–7323. <https://doi.org/10.1088/0953-8984/7/37/005>.
- (11) Kudo, A.; Keiko Omori; Kato, H. A Novel Aqueous Process for Preparation of Crystal Form-Controlled and Highly Crystalline BiVO₄ Powder from Layered Vanadates at Room Temperature and Its Photocatalytic and Photophysical Properties. **1999**, No. 14, 11459–11467. <https://doi.org/10.1021/JA992541Y>.
- (12) Bhattacharya, a K. Phase Transition in BiVO₄. *Materials Letters* **1997**, *30* (January), 7–13. [https://doi.org/10.1016/S0167-577X\(96\)00162-0](https://doi.org/10.1016/S0167-577X(96)00162-0).
- (13) Xue, Y.; Wang, X. The Effects of Ag Doping on Crystalline Structure and Photocatalytic Properties of BiVO₄. *International Journal of Hydrogen Energy* **2015**, *40* (17), 5878–5888. <https://doi.org/10.1016/j.ijhydene.2015.03.028>.
- (14) Martinez Suarez, C.; Hernández, S.; Russo, N. BiVO₄ as Photocatalyst for Solar Fuels Production through Water Splitting: A Short Review. *Applied Catalysis A: General* **2015**, *504*, 158–170. <https://doi.org/10.1016/j.apcata.2014.11.044>.
- (15) Hu, S.; Xiang, C.; Haussener, S.; Berger, A. D.; Lewis, N. S. An Analysis of the Optimal Band Gaps of Light Absorbers in Integrated Tandem Photoelectrochemical Water-Splitting Systems. *Energy & Environmental Science* **2013**, *6* (10), 2984–2993. <https://doi.org/10.1039/C3EE40453F>.
- (16) Abdi, F. F.; Firet, N.; vandeKrol, R. Efficient BiVO₄ Thin Film Photoanodes Modified with Cobalt Phosphate Catalyst and W-Doping. *ChemCatChem* **2013**, *5* (2), 490–496. <https://doi.org/10.1002/cctc.201200472>.
- (17) Park, Y.; McDonald, K. J.; Choi, K.-S. Progress in Bismuth Vanadate Photoanodes for Use in Solar Water Oxidation. *Chemical Society Reviews* **2013**, 2321–2337. <https://doi.org/10.1039/c2cs35260e>.
- (18) Kim, T. W.; Ping, Y.; Galli, G. A.; Choi, K.-S. Simultaneous Enhancements in Photon Absorption and Charge Transport of Bismuth Vanadate Photoanodes for Solar Water Splitting. *Nature Communications* **2015**, *6*, 8769. <https://doi.org/10.1038/ncomms9769>.
- (19) McDonald, K. J.; Choi, K.-S. A New Electrochemical Synthesis Route for a BiOI Electrode and Its Conversion to a Highly Efficient Porous BiVO₄ Photoanode for Solar Water Oxidation. *Energy & Environmental Science* **2012**, *5* (9), 8553. <https://doi.org/10.1039/c2ee22608a>.
- (20) Kronawitter, C. X.; Vayssieres, L.; Shen, S.; Guo, L.; Wheeler, D. a.; Zhang, J. Z.; Antoun, B. R.; Mao, S. S. A Perspective on Solar-Driven Water Splitting with All-Oxide Hetero-Nanostructures. *Energy & Environmental Science* **2011**, *4* (10), 3889. <https://doi.org/10.1039/c1ee02186a>.
- (21) Cho, S.; Jang, J. W.; Lee, K. H.; Lee, J. S. Research Update: Strategies for Efficient Photoelectrochemical Water Splitting Using Metal Oxide Photoanodes. *APL Materials* **2014**, *2* (1). <https://doi.org/10.1063/1.4861798>.
- (22) Toma, F. M.; Cooper, J. K.; Kunzelmann, V.; McDowell, M. T.; Yu, J.; Larson, D. M.; Borys, N. J.; Abelyan, C.; Beeman, J. W.; Yu, K. M.; et al. Mechanistic Insights into Chemical and Photochemical Transformations of Bismuth Vanadate Photoanodes. *Nat Commun* **2016**, *7* (May), 12012. <https://doi.org/10.1038/ncomms12012>.
- (23) Ma, Y.; Pendlebury, S. R.; Reynal, A.; le Formal, F.; Durrant, J. R. Dynamics of Photogenerated Holes in Undoped BiVO₄ Photoanodes for Solar Water Oxidation. *Chemical Science* **2014**, *5* (8), 2964. <https://doi.org/10.1039/c4sc00469h>.
- (24) Sinclair, T. S.; Hunter, B. M.; Winkler, J. R.; Gray, H. B.; Astrid, M. M. Materials Horizons Factors a Ff Ecting Bismuth Vanadate Photoelectrochemical Performance †. **2015**, 22–24. <https://doi.org/10.1039/c4mh00156g>.
- (25) Zhou, M.; Bao, J.; Xu, Y.; Zhang, J.; Xie, J.; Guan, M.; Wang, C.; Wen, L.; Lei, Y.; Xie, Y. Photoelectrodes Based upon Mo:BiVO₄ Inverse Opals for Photoelectrochemical Water Splitting. *ACS Nano* **2014**, *8* (7), 7088–7098. <https://doi.org/10.1021/nn501996a>.
- (26) Saracco, G.; Barbero, G.; Hernández, S.; Alexe-ionscu, A. L. Non-Monotonic Dependence of the Current Density on the Thickness of the Photoactive Layer. *Journal of Electroanalytical Chemistry* **2017**, 788, 61–65. <https://doi.org/10.1016/j.jelechem.2017.01.069>.
- (27) Abdi, F. F.; Savenije, T. J.; May, M. M.; Dam, B.; Krol, R. Van De. The Origin of Slow Carrier

- Transport in BiVO₄ Thin Film Photoanodes : A Time-Resolved Microwave Conductivity Study. *J. Phys. Chem. Lett.* **2013**, *4*, 2752–2757. <https://doi.org/10.1021/jz4013257>.
- (28) Rettie, A. J. E.; Lee, H. C.; Marshall, L. G.; Lin, J.-F.; Capan, C.; Lindemuth, J.; McCloy, J. S.; Zhou, J.; Bard, A. J.; Mullins, C. B. Combined Charge Carrier Transport and Photoelectrochemical Characterization of BiVO₄ Single Crystals: Intrinsic Behavior of a Complex Metal Oxide. *Journal of the American Chemical Society* **2013**, *135* (30), 11389–11396. <https://doi.org/10.1021/ja405550k>.
- (29) Hilliard, S.; Friedrich, D.; Kressman, S.; Strub, H.; Artero, V.; Laberty-Robert, C. Solar-Water-Splitting BiVO₄ Thin-Film Photoanodes Prepared By Using a Sol-Gel Dip-Coating Technique . *ChemPhotoChem* **2017**, *1* (6), 273–280. <https://doi.org/10.1002/cptc.201700003>.
- (30) Kim, J. H.; Lee, J. S. BiVO₄-Based Heterostructured Photocatalysts for Solar Water Splitting: A Review. *Energy and Environment Focus* **2014**, *3* (4), 339–353. <https://doi.org/10.1166/eef.2014.1121>.
- (31) Bornoz, P.; Abdi, F. F.; Tilley, S. D.; Dam, B.; Van De Krol, R.; Graetzel, M.; Sivula, K. A Bismuth Vanadate-Cuprous Oxide Tandem Cell for Overall Solar Water Splitting. *Journal of Physical Chemistry C* **2014**, *118* (30), 16959–16966. <https://doi.org/10.1021/jp500441h>.
- (32) Ma, J. S.; Lin, L. Y.; Chen, Y. S. Facile Solid-State Synthesis for Producing Molybdenum and Tungsten Co-Doped Monoclinic BiVO₄ as the Photocatalyst for Photoelectrochemical Water Oxidation. *International Journal of Hydrogen Energy* **2019**, *44* (16), 7905–7914. <https://doi.org/10.1016/j.ijhydene.2019.02.077>.
- (33) Yu, J.; Kudo, A. Effects of Structural Variation on the Photocatalytic Performance of Hydrothermally Synthesized BiVO₄. *Advanced Functional Materials* **2006**, *16* (16), 2163–2169. <https://doi.org/10.1002/adfm.200500799>.
- (34) Thalluri, S. M.; Rojas, R. M.; Rivera, O. D.; Hernandez, S.; Russo, N.; Rodil, S. E. Chemically Induced Porosity on BiVO₄ Films Produced by Double Magnetron Sputtering to Enhance the Photo-Electrochemical Response. *Physical Chemistry Chemical Physics* **2015**, *17* (27), 17821–17827. <https://doi.org/10.1039/C5CP01561H>.
- (35) Chen, L.; Toma, F. M.; Cooper, J. K.; Lyon, A.; Lin, Y.; Sharp, I. D.; Ager, J. W. Mo-Doped BiVO₄ Photoanodes Synthesized by Reactive Sputtering. **2015**, 1066–1071. <https://doi.org/10.1002/cssc.201402984>.
- (36) Alarco, E.; Chen, L.; Hettick, M.; Mashouf, N.; Lin, Y.; Ager, J. W. BiVO₄ Thin Film Photoanodes Grown by Chemical Vapor Deposition. **2014**, 1651–1657. <https://doi.org/10.1039/c3cp53904k>.
- (37) Bielinski, A. R.; Lee, S.; Brancho, J. J.; Esarey, S. L.; Gayle, A. J.; Kazyak, E.; Sun, K.; Bartlett, B. M.; Dasgupta, N. P. Atomic Layer Deposition of Bismuth Vanadate Core-Shell Nanowire Photoanodes. *Chemistry of Materials* **2019**, *31* (9), 3221–3227. <https://doi.org/10.1021/acs.chemmater.9b00065>.
- (38) Kim, T. W.; Choi, K.-S. Nanoporous BiVO₄ Photoanodes with Dual-Layer Oxygen Evolution Catalysts for Solar Water Splitting. **2014**, *343* (February), 990–995.
- (39) Thalluri, S. M.; Martinez Suarez, C.; Hernández, S.; Bensaid, S.; Saracco, G.; Russo, N. Elucidation of Important Parameters of BiVO₄ Responsible for Photo-Catalytic O₂ Evolution and Insights about the Rate of the Catalytic Process. *Chemical Engineering Journal* **2014**, *245*, 124–132. <https://doi.org/10.1016/j.cej.2014.02.017>.
- (40) Thalluri, S. M.; Hernández, S.; Bensaid, S.; Saracco, G.; Russo, N. Green-Synthesized W- and Mo-Doped BiVO₄ Oriented along the {040} Facet with Enhanced Activity for the Sun-Driven Water Oxidation. *Applied Catalysis B: Environmental* **2016**, *180*, 630–636. <https://doi.org/10.1016/j.apcatb.2015.07.029>.
- (41) Wang, D.; Jiang, H.; Zong, X.; Xu, Q.; Ma, Y.; Li, G.; Li, C. Crystal Facet Dependence of Water Oxidation on BiVO₄ Sheets under Visible Light Irradiation. *Chemistry - A European Journal* **2011**, *17* (4), 1275–1282. <https://doi.org/10.1002/chem.201001636>.
- (42) Dall'Antonia, L. H.; de Tacconi, N. R.; Chanmanee, W.; Timmaji, H.; Myung, N.; Rajeshwar, K. Electrosynthesis of Bismuth Vanadate Photoelectrodes. *Electrochemical and Solid-State Letters* **2010**, *13* (5), D29. <https://doi.org/10.1149/1.3322641>.
- (43) Rossell, M. D.; Agrawal, P.; Borgschulte, A.; Hébert, C.; Passerone, D.; Erni, R. Direct Evidence of Surface Reduction in Monoclinic BiVO₄. *Chemistry of Materials* **2015**, *27* (10), 3593–3600. <https://doi.org/10.1021/cm504248d>.
- (44) Silversmit, G.; Depla, D.; Poelman, H.; Marin, G. B.; De Gryse, R. Determination of the V2p XPS Binding Energies for Different Vanadium Oxidation States (V⁵⁺ to V⁰⁺). *Journal of Electron Spectroscopy and Related Phenomena* **2004**, *135* (2–3), 167–175. <https://doi.org/10.1016/j.elspec.2004.03.004>.

- (45) Silversmit, G.; Depla, D.; Poelman, H.; Marin, G. B.; Gryse, R. De. An XPS Study on the Surface Reduction of V_2O_5 (0 0 1) Induced by Ar^+ Ion Bombardment. **2006**, *600*, 3512–3517. <https://doi.org/10.1016/j.susc.2006.07.006>.
- (46) Wang, S.; Chen, P.; Bai, Y.; Yun, J. H.; Liu, G.; Wang, L. New $BiVO_4$ Dual Photoanodes with Enriched Oxygen Vacancies for Efficient Solar-Driven Water Splitting. *Advanced Materials* **2018**, *30* (20), 1–7. <https://doi.org/10.1002/adma.201800486>.
- (47) Bai, S.; Li, Q.; Han, J.; Yang, X.; Shu, X.; Sun, J.; Sun, L.; Luo, R.; Li, D.; Chen, A. Photoanode of LDH Catalyst Decorated Semiconductor Heterojunction of $BiVO_4/CdS$ to Enhance PEC Water Splitting Efficiency. *International Journal of Hydrogen Energy* **2019**, *44* (45), 24642–24652. <https://doi.org/10.1016/j.ijhydene.2019.07.214>.
- (48) Bai, H.; Guan, P.; Qu, K.; Fan, W.; Wang, F.; Xu, D.; Ding, J.; Shi, W. Reasonable Regulation of Kinetics over $BiVO_4$ Photoanode by Fe–CoP Catalysts for Boosting Photoelectrochemical Water Splitting. *International Journal of Hydrogen Energy* **2019**, *44* (52), 28184–28193. <https://doi.org/10.1016/j.ijhydene.2019.09.024>.
- (49) Wu, J.; Chen, Y.; Pan, L.; Wang, P.; Cui, Y.; Kong, D.; Wang, L.; Zhang, X.; Zou, J. Applied Catalysis B : Environmental Multi-Layer Monoclinic $BiVO_4$ with Oxygen Vacancies and V^{4+} Species for Highly Efficient Visible-Light Photoelectrochemical Applications. *Applied Catalysis B: Environmental* **2018**, *221* (August 2017), 187–195. <https://doi.org/10.1016/j.apcatb.2017.09.031>.
- (50) Silversmit, G.; Depla, D.; Poelman, H.; Marin, G. B.; Gryse, R. De. Determination of the V^{2p} XPS Binding Energies for Different Vanadium Determination of the V^{2p} XPS Binding Energies for Different Vanadium Oxidation States (V^{5+} to V^{0+}). **2004**, No. April. <https://doi.org/10.1016/j.elspec.2004.03.004>.
- (51) Zhang, B.; Wang, L.; Zhang, Y.; Ding, Y.; Bi, Y. Ultrathin $FeOOH$ Nanolayers with Abundant Oxygen Vacancies on $BiVO_4$ Photoanodes for Efficient Water Oxidation. *Angewandte Chemie - International Edition* **2018**, *57* (8), 2248–2252. <https://doi.org/10.1002/anie.201712499>.
- (52) Zhang, Y.; Guo, Y.; Duan, H.; Li, H.; Sun, C. Facile Synthesis of V^{4+} Self-Doped, [010] Oriented $BiVO_4$ Nanorods with Highly Efficient Visible Light-Induced Photocatalytic Activity. *Phys. Chem. Chem. Phys.* **2014**, *16*, 24519–24526. <https://doi.org/10.1039/c4cp03795b>.
- (53) Sayama, K.; Nomura, A.; Arai, T.; Sugita, T.; Abe, R.; Oi, T.; Iwasaki, Y.; Abe, Y.; Sugihara, H. Photoelectrochemical Decomposition of Water into H_2 and O_2 on Porous $BiVO_4$ Thin-Film Electrodes under Visible Light and Significant Effect of Ag Ion Treatment Photoelectrochemical Decomposition of Water into H_2 and O_2 on Porous $BiVO_4$ Thin-Film Electrode. *The Journal of Physical Chemistry B* **2006**, *3*, 11352–11360. <https://doi.org/10.1021/jp057539>.
- (54) Passerone, D.; Erni, R. Direct Evidence of Surface Reduction in Monoclinic $BiVO_4$. **2015**. <https://doi.org/10.1021/cm504248d>.
- (55) Lee, D. K.; Choi, K. S. Enhancing Long-Term Photostability of $BiVO_4$ Photoanodes for Solar Water Splitting by Tuning Electrolyte Composition. *Nature Energy* **2018**, *3* (1), 53–60. <https://doi.org/10.1038/s41560-017-0057-0>.
- (56) Kim, T. W.; Choi, K.-S. Nanoporous $BiVO_4$ Photoanodes with Dual-Layer Oxygen Evolution Catalysts for Solar Water Splitting. *Science* **2014**, *343* (6174), 990–994. <https://doi.org/10.1126/science.1246913>.
- (57) Banerjee, A. N.; Kundoo, S.; Saha, P.; Chattopadhyay, K. K. Synthesis and Characterization of Nano-Crystalline Fluorine-Doped Tin Oxide Thin Films by Sol-Gel Method. *Journal of Sol-Gel Science and Technology* **2003**, *28* (1), 105–110. <https://doi.org/10.1023/A:1025697322395>.
- (58) Gim, S.; Bisquert, J.; Principles, F. B.; Devices, A. *Photoelectrochemical Solar Fuel Production*; **2016**. <https://doi.org/10.1007/978-3-319-29641-8>.

Appendix A. Supplementary data

The following are the Supplementary data to this article:

Optimization of BiVO₄ photoelectrodes made by electrodeposition for sun-driven water oxidation

Kristine Rodulfo Tolod^{1,2}, Simelys Hernández^{1,*}, Micaela Castellino¹, Fabio Alessandro Deorsola¹, Elahe Davarpanah¹ and Nunzio Russo¹

¹Department of Applied Science and Technology, Politecnico di Torino,
Corso Duca degli Abruzzi, 10129 Turin, Italy

²Université de Lyon, Institut de Chimie de Lyon, Laboratory of Chemistry, Catalysis, Polymers and Processes (C2P2, UMR 5265 - CNRS - University Claude Bernard Lyon 1 - Ecole Supérieure de Chimie Physique et Procédé CPE Lyon), Villeurbanne, France

*E-mail of corresponding author: simelys.hernandez@polito.it

Supporting Information

SI 1. Preliminary experiments for factor screening

Initially, 6 factors have been identified and preliminarily screened in order to identify the significant factors to be subjected to design of experiments. The factors that were investigated were: potential, electrodeposition time, Bi-KI to benzoquinone-ethanol ratio, V precursor solvent, calcination temperature and ramp rate.

S1.1 Effect of Potential

With all other factors held constant, the effect of potential (-0.05V to -2V vs Ag/AgCl (3M KCl)) was investigated. Electrodeposition time was set at 3 min and Bi-KI to benzoquinone-ethanol ratio of 2.5.

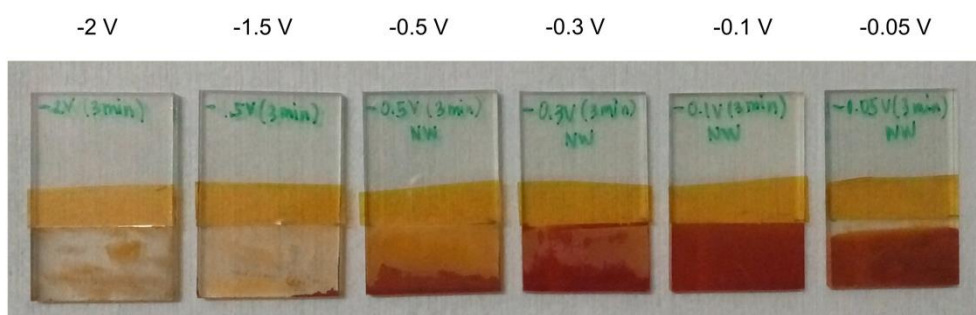


Figure SI-1. Electrodeposition with varying potentials

As seen in Figure S1, deposition was accomplished with a uniform coverage of the electrode at a potential of -0.1V vs Ag/AgCl (3M KCl). Depositing at higher potentials did not yield a film that adhered to the FTO surface while using a lower potential did not entirely cover the set electrodeposition area. For this reason, the applied potential was fixed at -0.1V vs Ag/AgCl (3M KCl) for the experimental runs.

S1.2 Effect of electrodeposition time

Varying the electrodeposition time varies the thickness of electrodeposited films, as shown in Figure S2. For the design of experiments, a wider range of electrodeposition time, from 0.5 min to 10 min, has been considered.

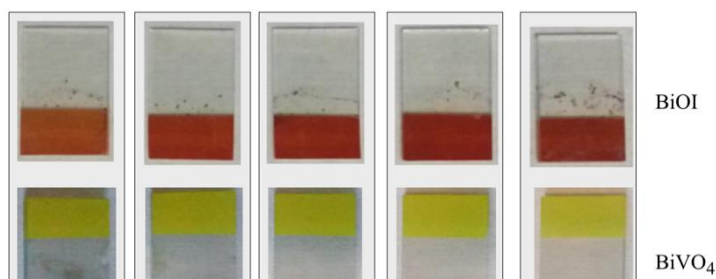


Figure SI-2. Electrodeposited BiOI (TOP) and synthesized BiVO₄ (BOTTOM) at different electrodeposition times, (Bi-KI to benzoquinone-ethanol ratio at 2.5 and the calcination temperature of 450°C)

S1.3 Effect of the Bi-KI to Benzoquinone-ETOH ratio

The electrodeposition of BiOI onto the FTO glass is made possible by the reduction of p-benzoquinone to hydroquinone. The p-benzoquinone consumes H^+ in the solution during the process, which results in a local pH increase enabling the precipitation of BiOI on the FTO glass working electrode.⁵⁵

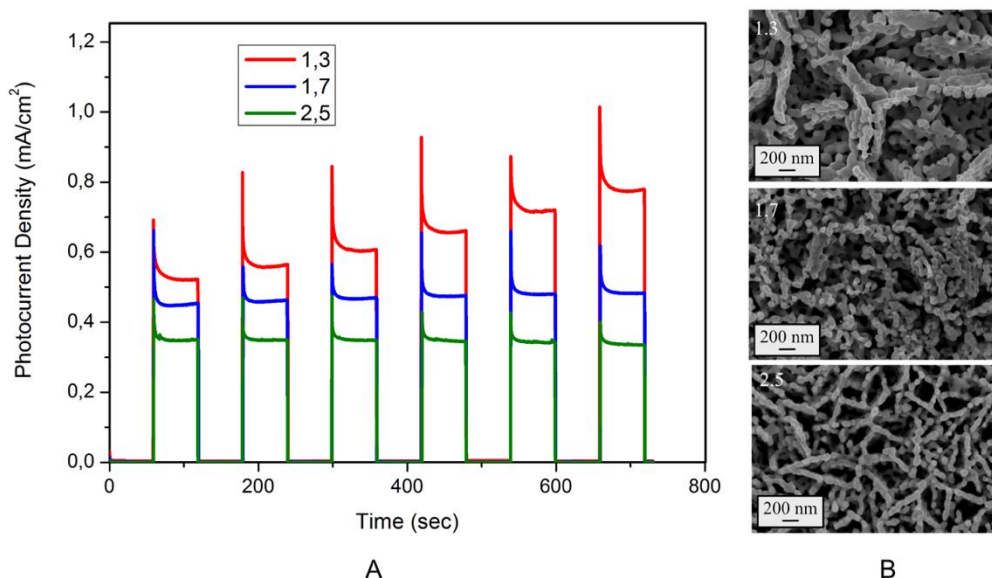


Figure SI-3. Water oxidation activity results by varying the Bi-KI to benzoquinone-EtOH ratio. (A) Chronoamperometry plots of the photocurrent density and the (B) corresponding FE-SEM images, (electrodeposition time of 3 minutes and calcination temperature of 450 °C)

The ratios investigated for the Bi-KI to benzoquinone-ethanol are 1.3 to 2.5 because differences in morphology were observed among the samples synthesized at different ratios in the preliminary tests. At a ratio of 1, no deposition was observed.

S1.4 Effect of the Vanadium precursor solvent

Two V precursor solvents were initially used. The photocurrent densities obtained using DMSO (dimethyl sulfoxide) were slightly higher than those using DMF (dimethylfuran). For this reason and due to the safety considerations, the V precursor solvent chosen was DMSO.

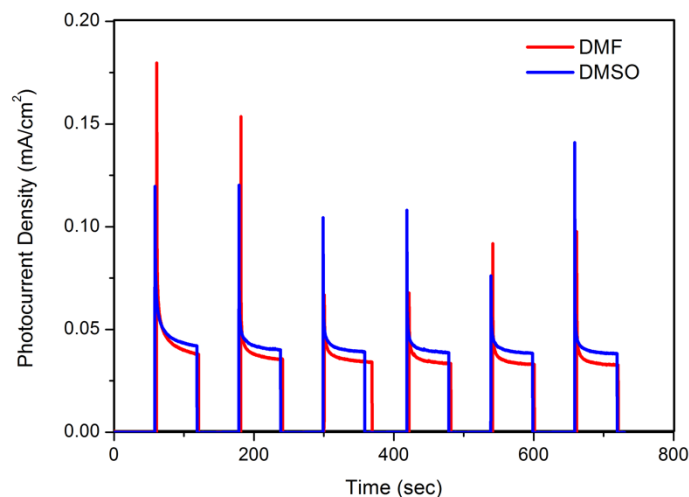


Figure SI-4. Chronoamperometry plot showing the effect of the Vanadium precursor solvent on the photocurrent density (electrodeposition time of 3 minutes and calcination temperature of 450 °C)

S1.5 Effect of the calcination temperature

Significant morphology changes as well as different grain sizes were observed upon calcination at the temperature range of 350°C to 500°C. This was the same range that was employed in the design of experiments.

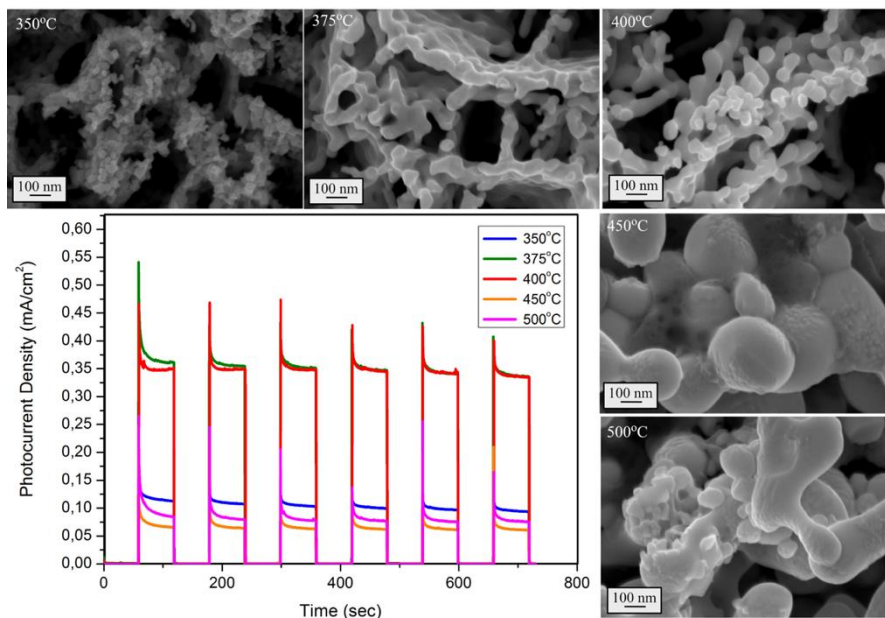


Figure SI-5. Chronoamperometry plot showing the effect of calcination temperature on the photocurrent density and the resulting morphologies, as shown by the FE-SEM images (electrodeposition time of 3 minutes and Bi-KI to benzoquinone-EtOH ratio of 2.5)

S1.6 Effect of the calcination heating rate

A fast (20°C) and slow (2°C) ramp rate were preliminarily tested to identify the effect of heating rate during calcination on the morphology and photocurrent density of the material. Based on preliminary tests, a slower ramp rate is preferred, thus, the heating rate was fixed to 2°C/min.

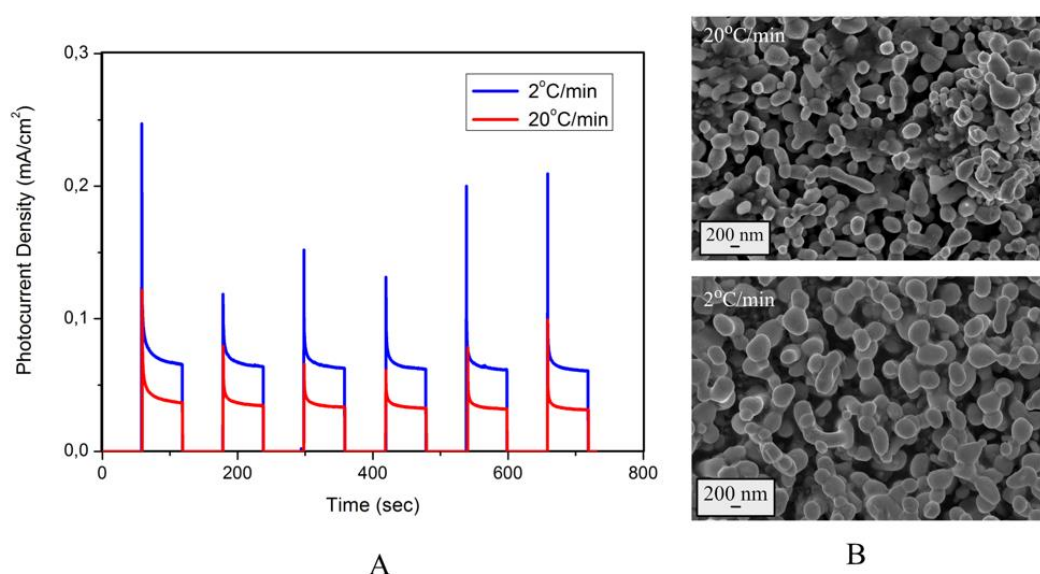


Figure SI-6. Water oxidation activity results by varying calcination heating/ramp rate. (A) Chronoamperometry plot showing the photocurrent density and the (B) corresponding FE-SEM images, (electrodeposition time of 3 minutes and calcination temperature of 450 °C)

SI 2. Preparation of BiVO₄ photoanodes

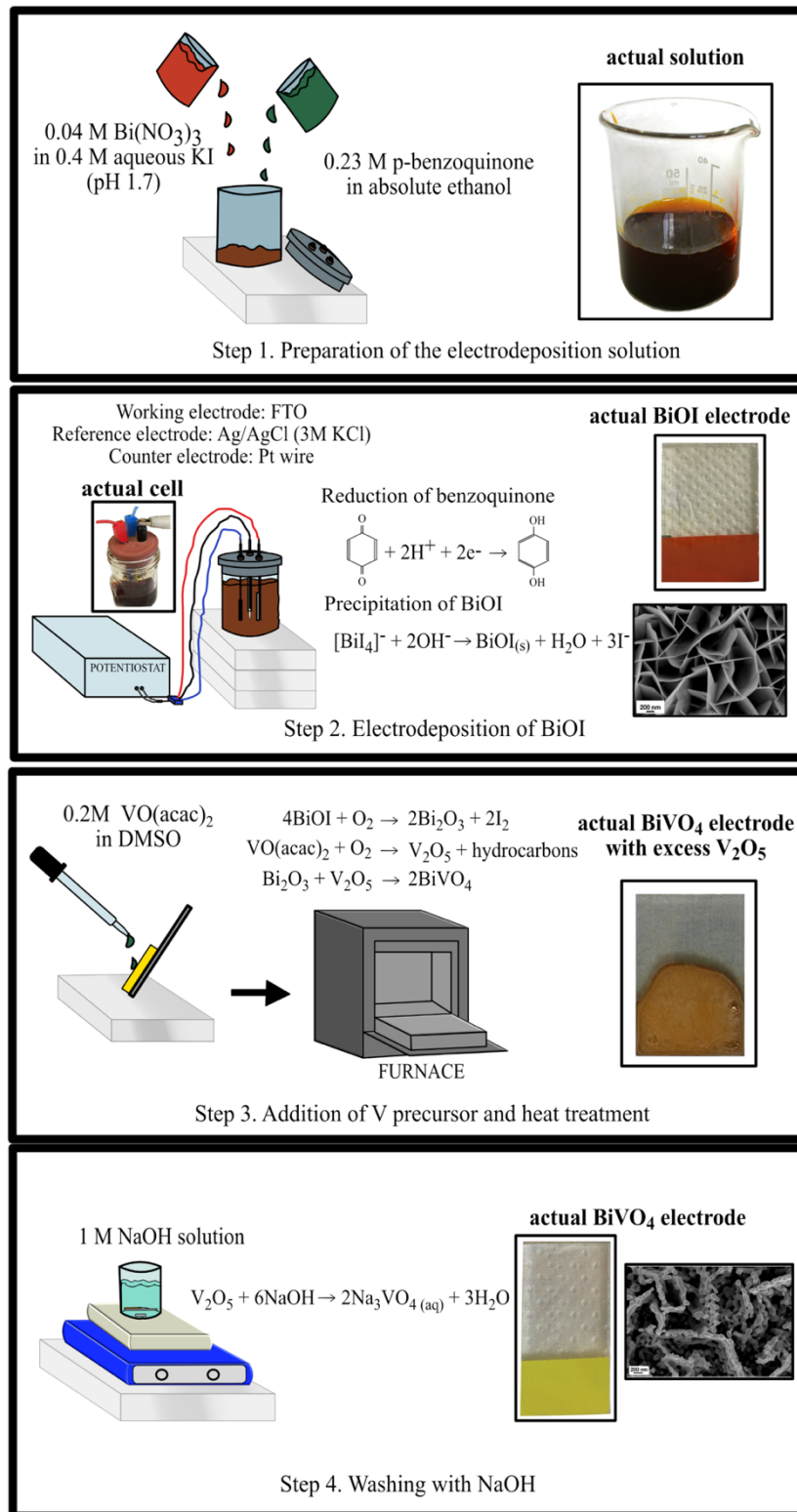


Figure SI-7. Synthesis of pristine BiVO₄

SI 3. Factors optimized using the experimental design

Table SI-1. Important factors that were optimized using the experimental design

Factor	Levels		Electro-deposition time (min)	Fixed factor	
	Min	Max		Calcination temperature (°C)	Bi-KI to benzoquinone-EtOH ratio
Electrodeposition time (min)	0.5	10	---	425	1.9
Calcination temperature (°C)	350	500	5.25	---	1.9
Bi-KI to benzoquinone-EtOH ratio	1.3	2.5	5.25	425	---

SI 4. FE-SEM images of BiVO₄ photoanodes

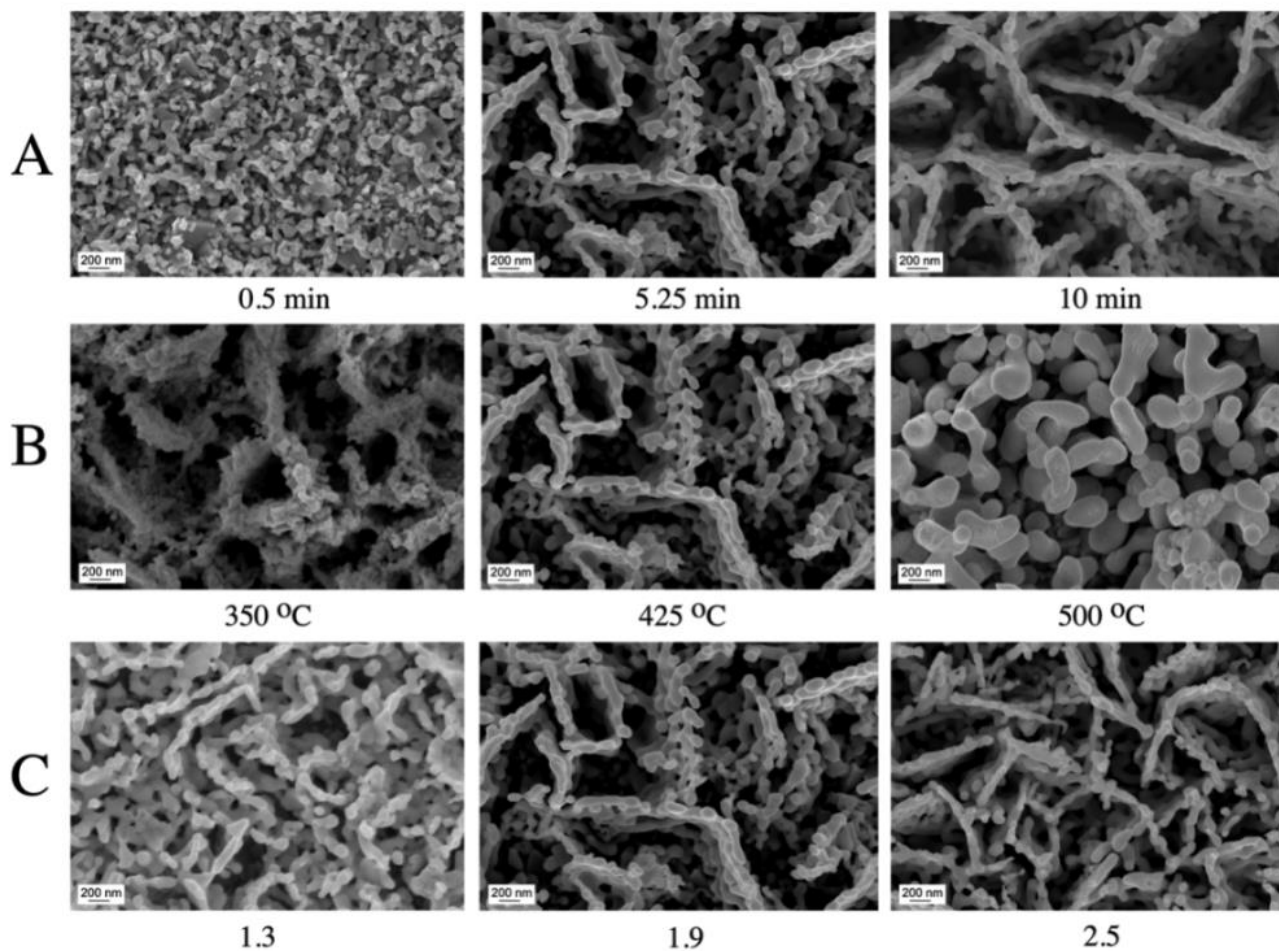
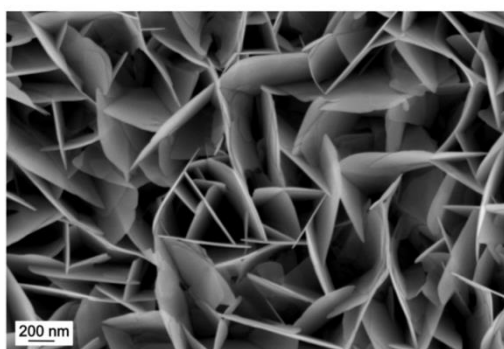
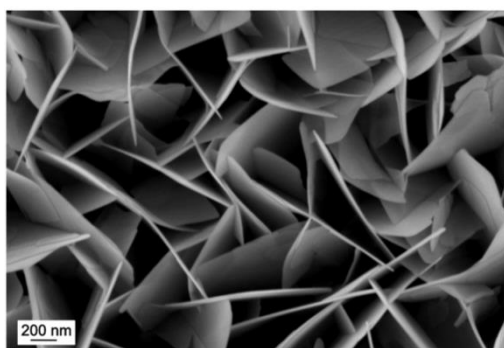


Figure SI-8. FE-SEM images of the bare BiVO₄ photoanodes synthesized at different: (A) electrodeposition times, (B) calcination temperatures, and (C) Bi-KI to Benzoquinone-EtOH ratio, as detailed in SI 3. **Factors optimized using the experimental design**

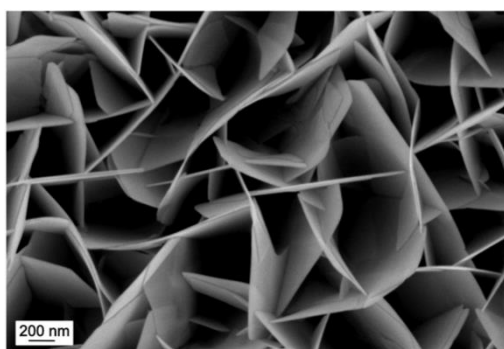
SI 5. FE-SEM images of BiOI



1 min



3 min



5 min

Figure SI-9. FE-SEM Images of electrodeposited BiOI at different electrodeposition time
(1 min, 3min, and 5 min)

SI 6. XRD Spectra

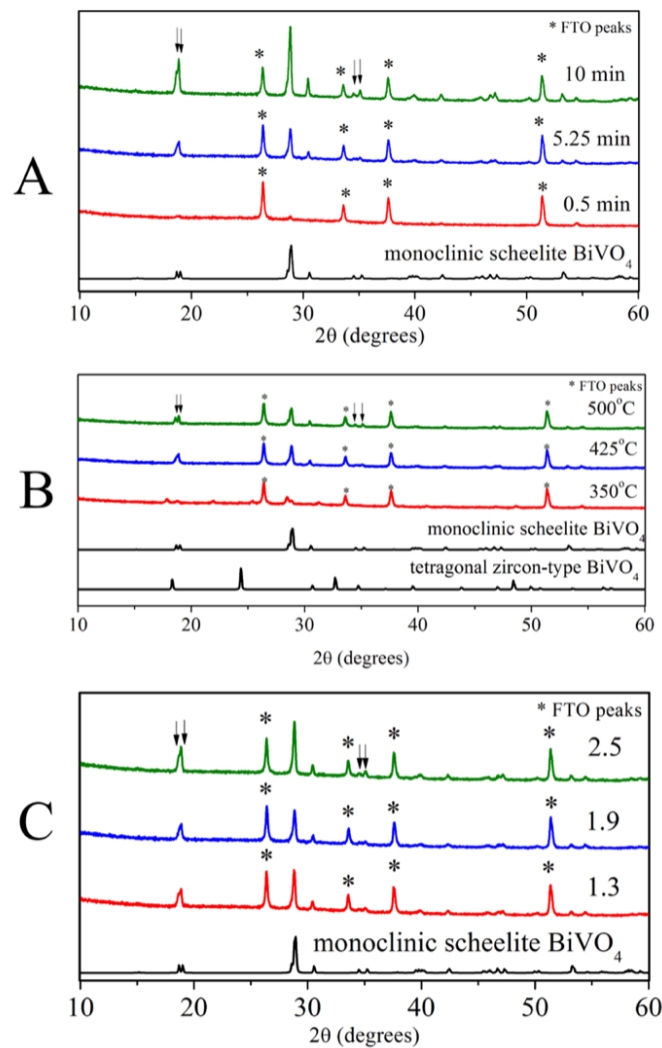


Figure SI-10. XRD spectra of the bare BiVO_4 photoanodes synthesized at different: (a) electrodeposition times, (b) calcination temperatures, and (c) Bi-KI to Benzoquinone-EtOH ratio, as specified in SI 3. **Factors optimized using the experimental design**

Table SI-1.

SI 7. UV-vis diffuse reflectance spectra

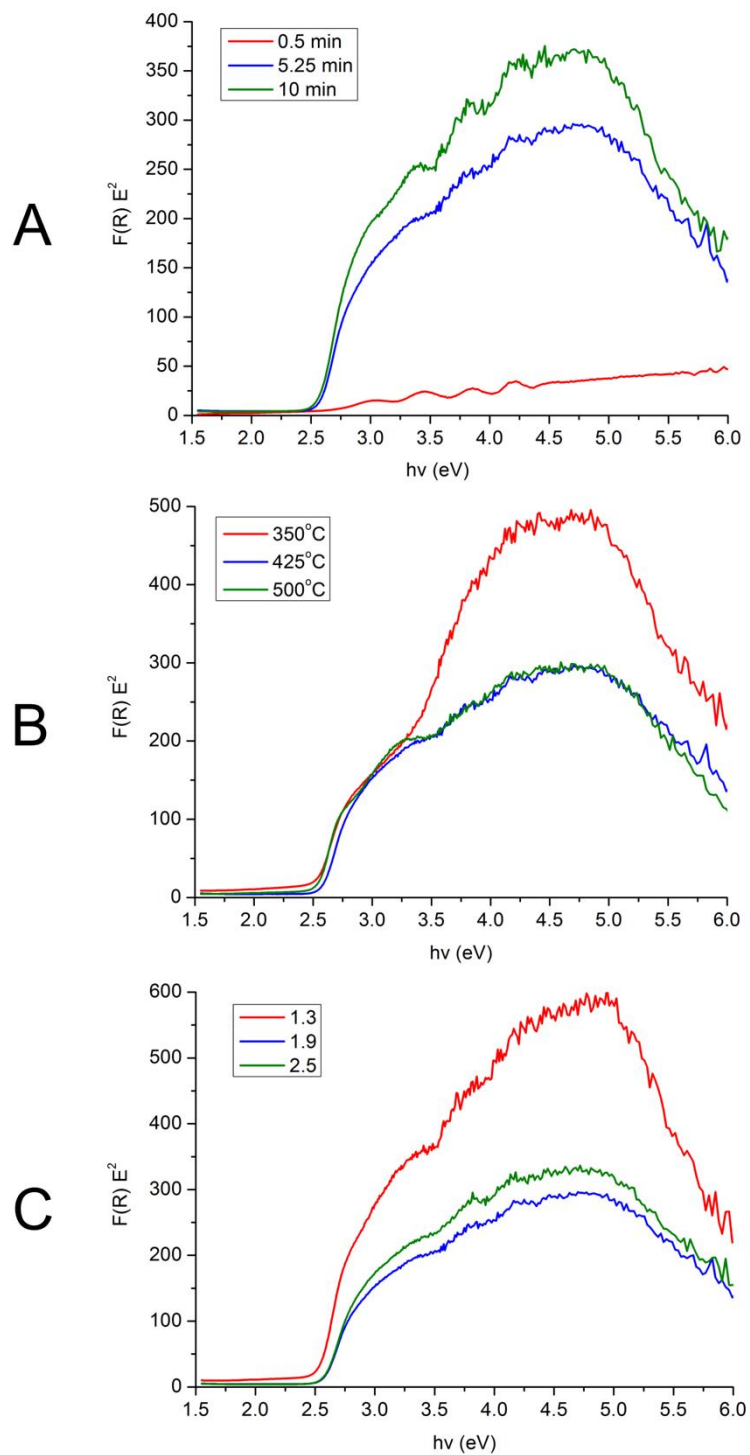


Figure SI-11. Kubelka-Munk function versus photon energy at various (A) electrodeposition time, (B) calcination temperature, and (C) Bi-KI to benzoquinone-EtOH ratio

SI 8. Summary of physico-chemical properties

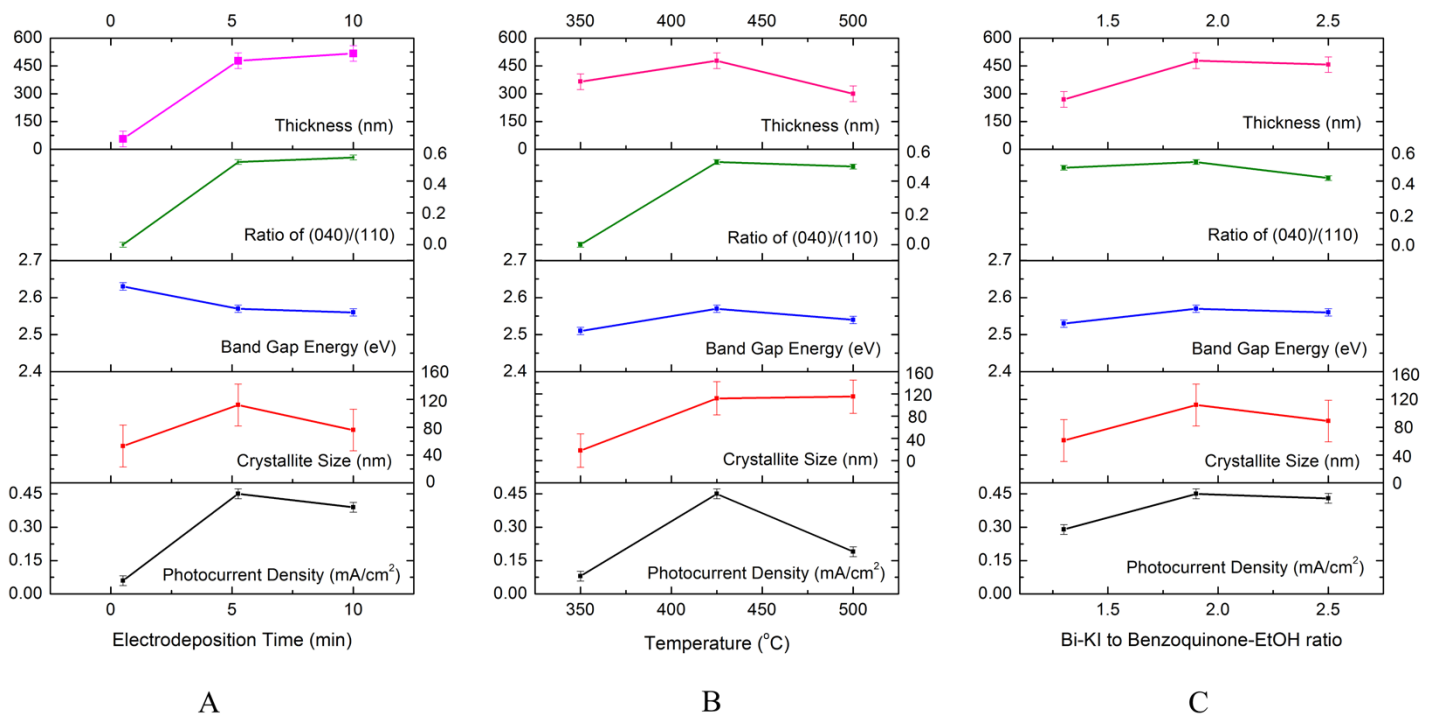


Figure SI-12. Summary of physico-chemical properties at various (A) electrodeposition time, (B) calcination temperature, and (C) Bi-KI to benzoquinone-EtOH ratio, plotted with respect to the photocurrent density

SI 9. XPS spectra and bulk/surface Bi/V ratios

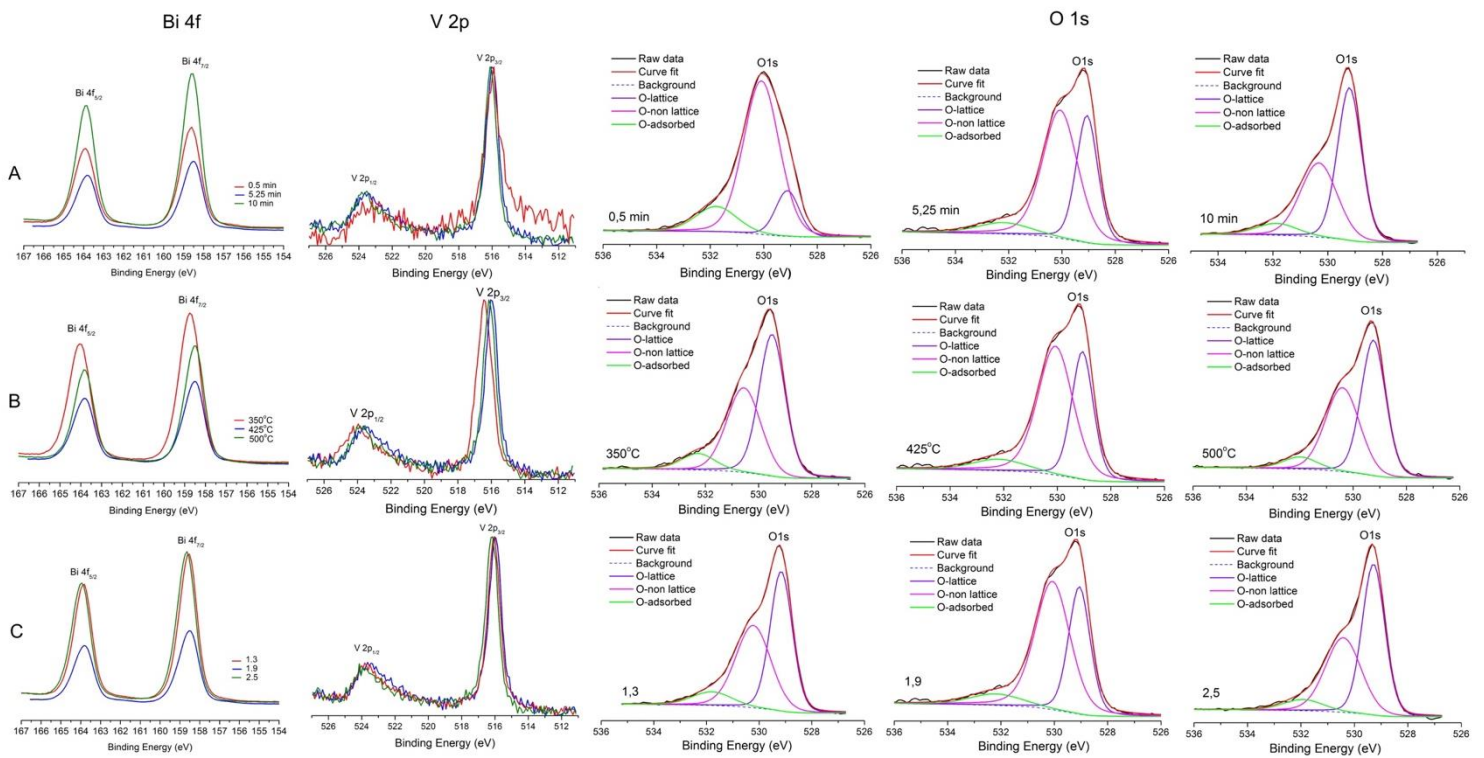


Figure SI-13. Bi4f, V2p, and O1s XPS spectra for electrodes after testing with various (A) electrodeposition time, (B) calcination temperature, and (C) Bi-KI to benzoquinone-EtOH ratio

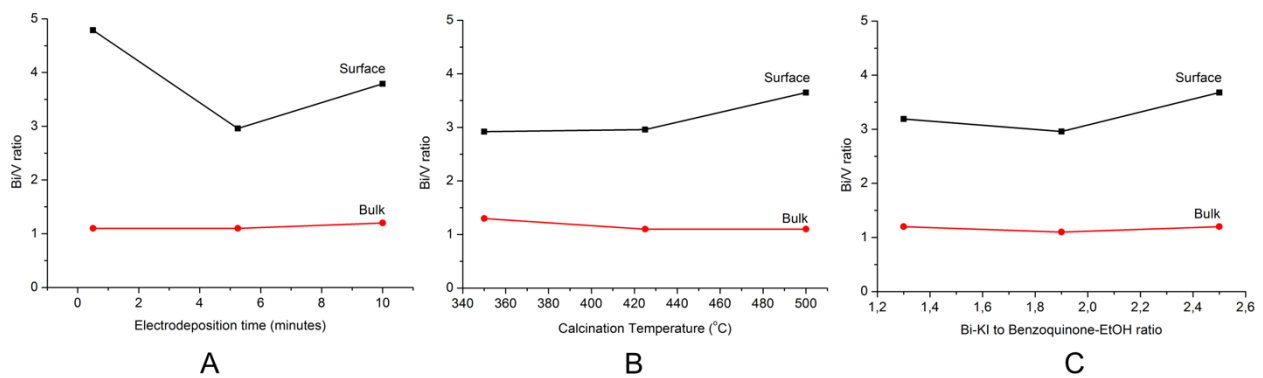


Figure SI-14. Surface and bulk Bi/V ratio of electrodes after testing with different (A) electrodeposition time, (B) calcination temperature, and (C) Bi-KI to benzoquinone-EtOH ratio

SI 10. Mott-Schottky plots

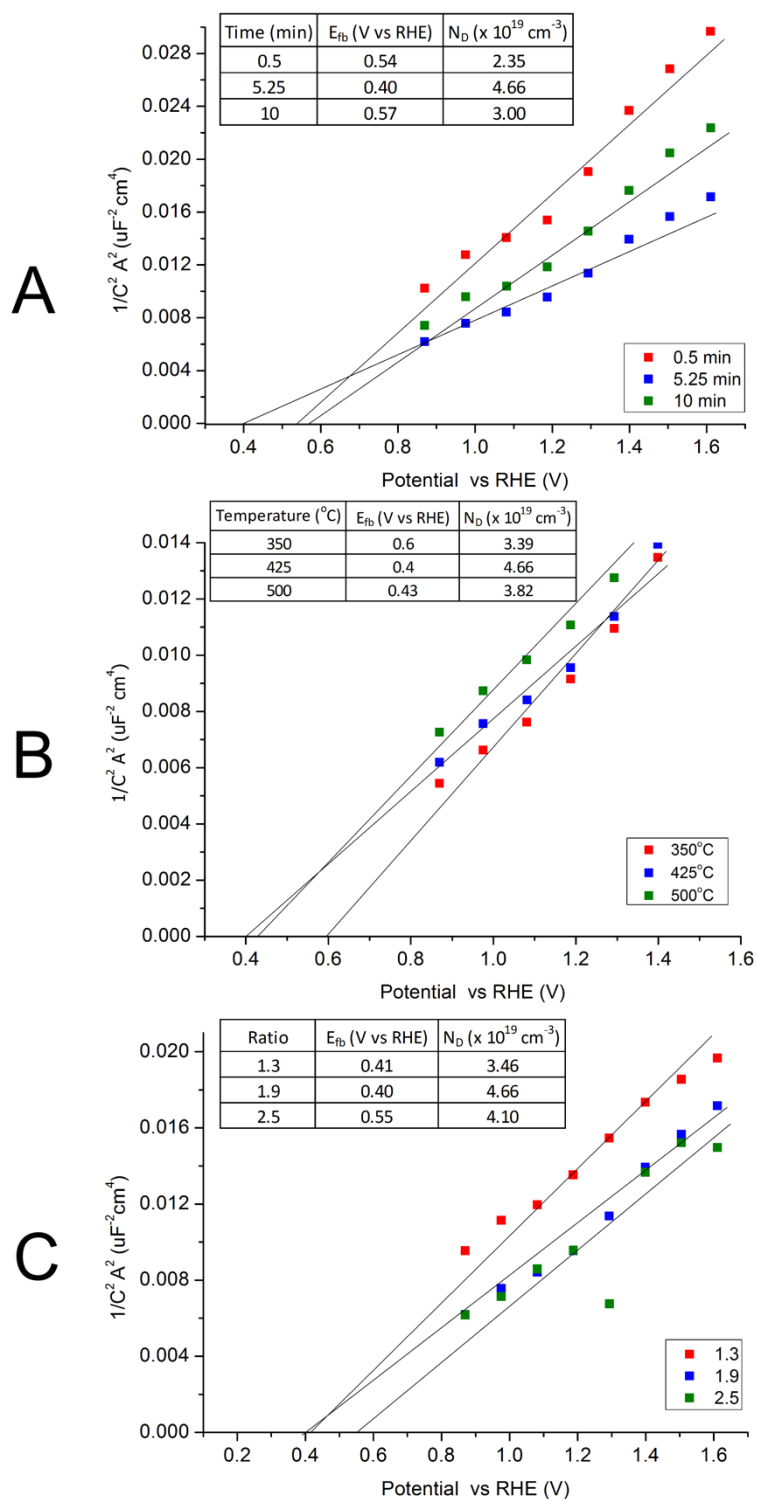


Figure SI-15. Mott-Schottky plots at various (A) electrodeposition time, (B) calcination temperature, and (C) Bi-KI to benzoquinone-EtOH ratio, measured at 7.6 kHz

SI 11. Onset potentials

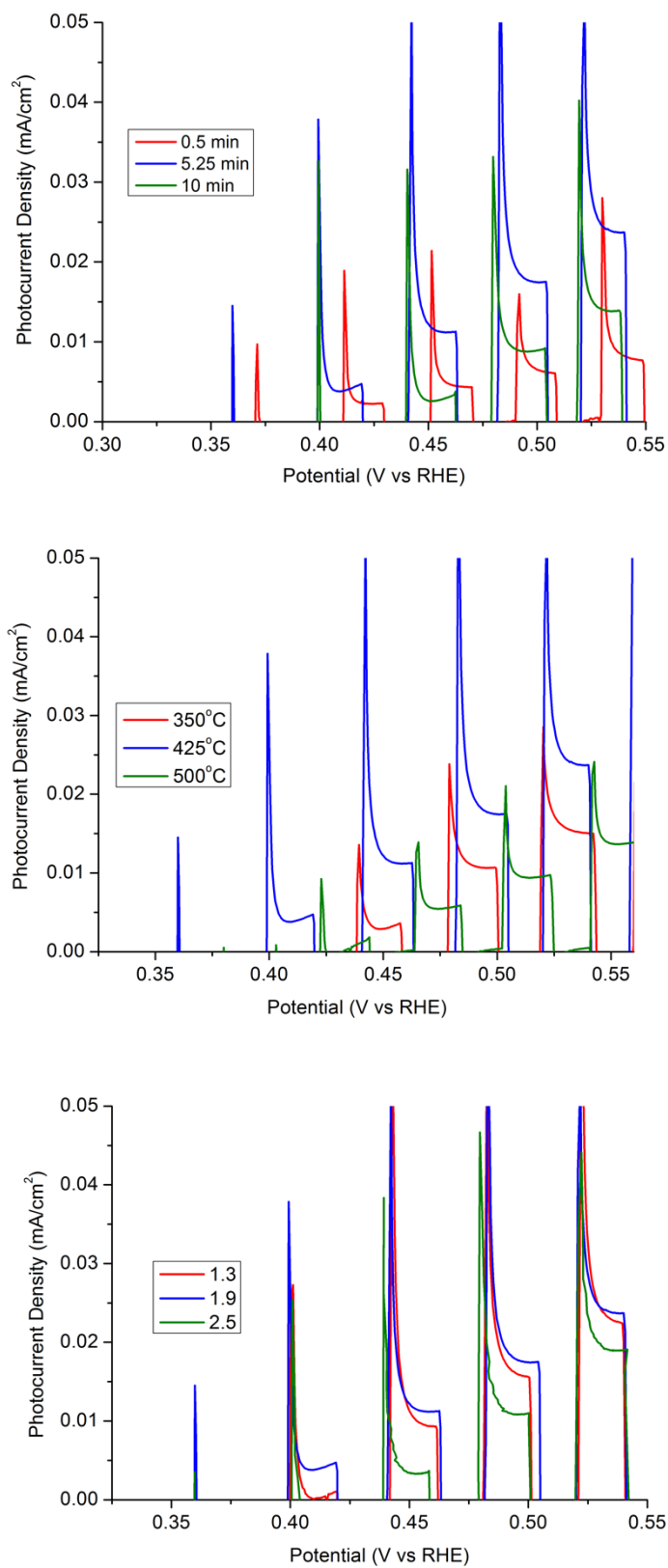


Figure SI-16. Magnified LSV plots showing the region of onset potentials

SI 12. Equivalent circuit model and calculated charge transfer resistances

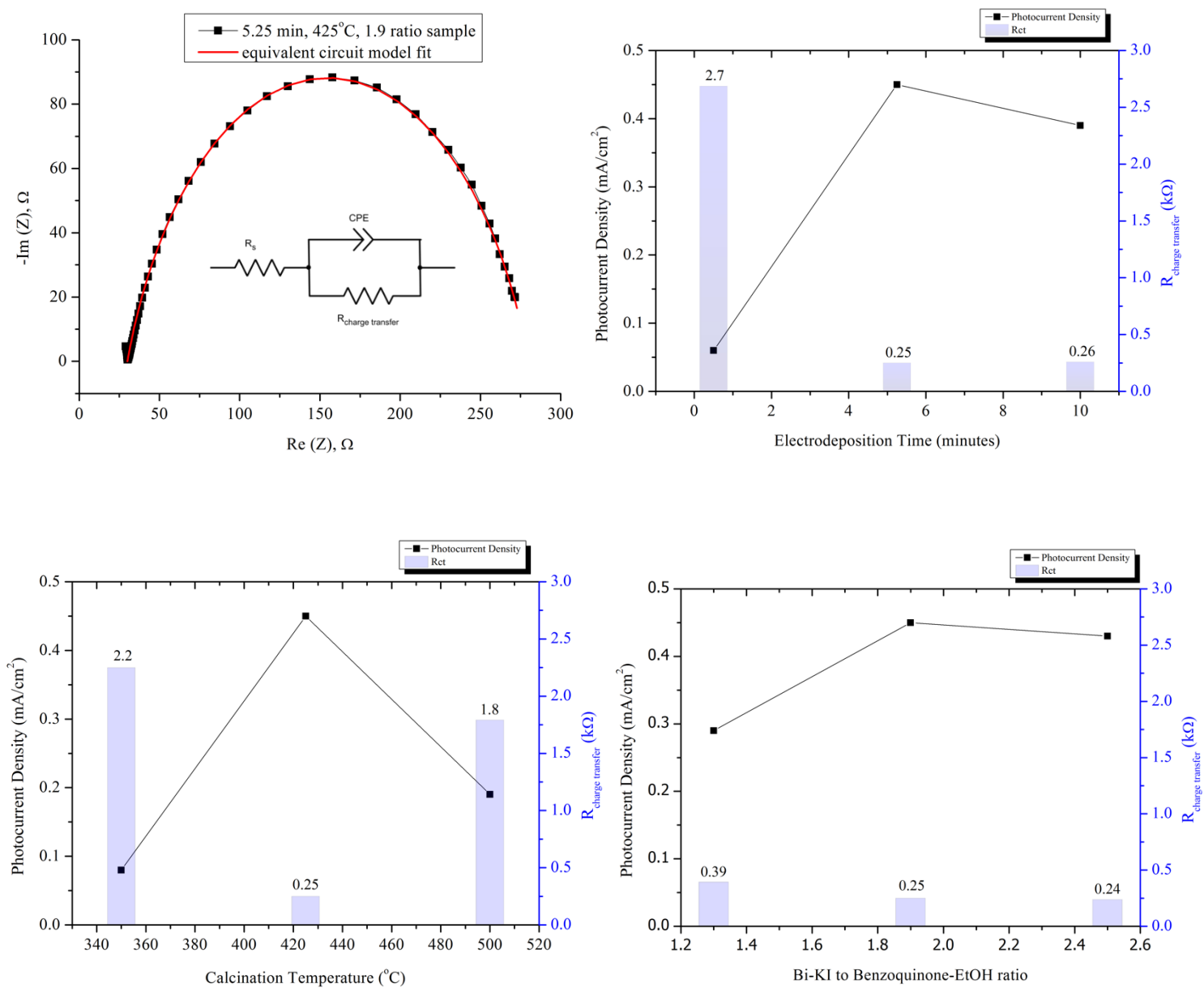


Figure SI-17. Model of the equivalent circuit and the plots of the calculated charge transfer resistances versus photocurrent density